






Iron-rich Metal-poor Stars and the Astrophysics of Thermonuclear Events Observationally Classified as Type Ia Supernovae. I. Establishing the Connection

Henrique Reggiani^{1,5} , Kevin C. Schlaufman² , and Andrew R. Casey^{3,4} 

¹The Observatories of the Carnegie Institution for Science, 813 Santa Barbara Street, Pasadena, CA 91101, USA; hreggiani@carnegiescience.edu

²William H. Miller III Department of Physics & Astronomy, Johns Hopkins University, 3400 N. Charles Street, Baltimore, MD 21218, USA

³School of Physics & Astronomy, Monash University, Wellington Road, Clayton 3800, Victoria, Australia

⁴ARC Centre of Excellence for All Sky Astrophysics in 3 Dimensions (ASTRO 3D), Canberra, ACT 2611, Australia

Received 2023 January 31; revised 2023 March 20; accepted 2023 March 23; published 2023 August 25

Abstract

The progenitor systems and explosion mechanisms responsible for the thermonuclear events observationally classified as Type Ia supernovae are uncertain and difficult to uniquely constrain using traditional observations of Type Ia supernova host galaxies, progenitors, light curves, and remnants. For the subset of thermonuclear events that are prolific producers of iron, we use published theoretical nucleosynthetic yields to identify a set of elemental abundance ratios infrequently observed in metal-poor stars but shared across a range of progenitor systems and explosion mechanisms: $[\text{Na}, \text{Mg}, \text{Co}/\text{Fe}] < 0$. We label stars with this abundance signature “iron-rich metal-poor,” or IRMP stars. We suggest that IRMP stars formed in environments dominated by thermonuclear nucleosynthesis and consequently that their elemental abundances can be used to constrain both the progenitor systems and explosion mechanisms responsible for thermonuclear explosions. We identify three IRMP stars in the literature and homogeneously infer their elemental abundances. We find that the elemental abundances of BD +80 245, HE 0533–5340, and SMSS J034249.53–284216.0 are best explained by the (double) detonations of sub-Chandrasekhar-mass CO white dwarfs. If our interpretation of IRMP stars is accurate, then they should be very rare in globular clusters and more common in the Magellanic Clouds and dwarf spheroidal galaxies than in the Milky Way’s halo. We propose that future studies of IRMP stars will quantify the relative occurrences of different thermonuclear event progenitor systems and explosion mechanisms.

Unified Astronomy Thesaurus concepts: Chemically peculiar stars (226); Explosive nucleosynthesis (503); Dwarf spheroidal galaxies (420); Globular star clusters (656); Magellanic Clouds (990); Milky Way stellar halo (1060); Big Bang nucleosynthesis (151); Nucleosynthesis (1131); Stellar nucleosynthesis (1616); Population II stars (1284); Stellar abundances (1577); Type Ia supernovae (1728)

Supporting material: machine-readable table

1. Introduction

Several lines of observational evidence support the conclusion that Type Ia supernovae are produced by the thermonuclear explosions of carbon–oxygen (CO) white dwarfs left behind as the embers of $1 M_{\odot} \lesssim M_{*} \lesssim 8 M_{\odot}$ stars (e.g., Whelan & Iben 1973). Unlike Type Ib/c and Type II supernovae that are only observed in star-forming galaxies and thought to result from the explosions of massive stars, Type Ia supernovae are observed in both star-forming and passively evolving galaxies (Zwicky 1958). The lack of hydrogen and helium lines in the spectra of Type Ia supernovae points to degenerate objects, while lines of silicon, calcium, and iron blueshifted by 10^4 km s^{-1} indicate explosions and the presence of significant amounts of both intermediate-mass and iron-peak elements (e.g., Hoyle & Fowler 1960; Branch et al. 1983, 1985; Kirshner et al. 1993; Mazzali et al. 1993). The fusion of carbon and oxygen at high absolute densities and temperatures can produce at relatively low densities intermediate-mass elements and at relatively high densities iron-peak elements like radioactive ^{56}Ni in nuclear

statistical equilibrium. The energy thereby released is sufficient to unbind a CO white dwarf with $M_{\text{WD}} \approx 1 M_{\odot}$ and accelerate a typical Type Ia supernova ejecta mass to 10^4 km s^{-1} (e.g., Arnett 1969; Maoz et al. 2014). The characteristic few-week rise to maximum light followed by an order-of-magnitude decline in 1 month and then less rapid decline thereafter is well explained by the radioactive decays $^{56}\text{Ni} \rightarrow ^{56}\text{Co} \rightarrow ^{56}\text{Fe}$ (e.g., Pankey 1962; Colgate & McKee 1969). Observations of Galactic supernova remnants left behind by Type Ia supernovae support this picture (e.g., Minkowski 1964; Badenes et al. 2006).

There are now highly refined models of several progenitor systems and explosion mechanisms that are broadly consistent with observed Type Ia supernova host galaxies, progenitors, light curves, and remnants (e.g., Hillebrandt et al. 2013). While this broad model consistency with observational data represents an impressive achievement of theoretical astrophysics, no single progenitor system and explosion mechanism explains all Type Ia supernovae (e.g., Hoefflich & Khokhlov 1996; Nugent et al. 1997). Most models invoke thermonuclear explosions of CO white dwarfs due to interactions with binary companions. In the single-degenerate scenario, a thermonuclear supernova results from a CO white dwarf’s binary interactions with a star leaving the main sequence, on the giant branch, or that has lost its hydrogen envelope. In the double-degenerate scenario, a thermonuclear supernova results from a CO white dwarf’s interactions with another white dwarf. In either the single-

⁵ Carnegie Fellow.

degenerate or double-degenerate scenarios, the CO white dwarf producing a thermonuclear explosion may be near the Chandrasekhar mass $1.3 M_{\odot} \lesssim M_{\text{Ch}} \lesssim 1.4 M_{\odot}$ (e.g., Leung & Nomoto 2018) or significantly below the Chandrasekhar mass (i.e., sub- M_{Ch}).

Preceded by approximately 100 yr of convective carbon burning usually called simmering (e.g., Nomoto et al. 1984; Piro & Bildsten 2008; Piro & Chang 2008; Piro 2008; Schwab et al. 2017), the thermonuclear explosions of near- M_{Ch} CO white dwarfs accreting hydrogen can in principle proceed as pure detonations, pure deflagrations, or delayed detonations. Pure detonations are thought to produce copious amounts of iron-peak elements but too little intermediate-mass elements to explain the lines of those species in Type Ia supernovae (Arnett et al. 1971). They are also too bright to explain most Type Ia supernova light curves. In a pure deflagration, carbon fusion ignited in the interior of a white dwarf moves toward the surface as the energy released is conducted outward by the degenerate electron gas (Nomoto et al. 1976, 1984). The energy causes the white dwarf to expand, allowing for the production of both iron-peak elements in dense regions and intermediate-mass elements in less dense regions. In a delayed detonation, subsonic transport of energy outward from the deflagration causes an expansion of the white dwarf before a following supersonic detonation wave unbinds the white dwarf and produces nucleosynthesis that does not reach the iron peak in relatively low density environments (Khokhlov 1991). This delayed detonation can occur as a deflagration-to-detonation transition (DDT; Gamezo et al. 2003, 2004, 2005; Röpke & Niemeyer 2007; Bravo & García-Senz 2008; Seitzzahl et al. 2011), a gravitationally confined detonation (GCD; Plewa et al. 2004; Jordan et al. 2008, 2012), or a pulsational reverse detonation (PRD; Bravo & García-Senz 2009; Bravo et al. 2009). All of these explosion mechanisms operate for near- M_{Ch} CO white dwarfs in single-degenerate systems.

The thermonuclear explosion of a sub- M_{Ch} CO white dwarf accreting helium can proceed as a double detonation (Nomoto 1982a, 1982b; Woosley et al. 1986; Livne 1990; Fink et al. 2007, 2010; Woosley & Kasen 2011). In a double detonation, the compression of a helium envelope resulting from accretion can spark a detonation in the helium envelope that produces intermediate-mass elements. That first detonation creates a shock wave in the bulk of the white dwarf that subsequently sparks a detonation in the interior and produces iron-peak elements. The sub- M_{Ch} CO white dwarf can accrete the helium shell necessary for a double detonation from the helium core remaining after its companion star loses its hydrogen envelope. Accretion from a helium white dwarf companion is also possible, either stably (e.g., Bildsten et al. 2007) or dynamically (e.g., Webbink 1984; Guillochon et al. 2010; Pakmor et al. 2013). Double detonations can therefore occur in both the single-degenerate and double-degenerate scenarios.

Thermonuclear explosions of both M_{Ch} and sub- M_{Ch} CO white dwarfs can also be attributed to detonations resulting from violent mergers (e.g., Yoon et al. 2007; Rosswog et al. 2009; Pakmor et al. 2010, 2011, 2012). These violent mergers can occur in dense stellar environments or as a result of secular eccentricity excitation in triple systems (Thompson 2011; Kushnir et al. 2013). Thermonuclear explosions of this type only occur through the double-degenerate scenario.

Despite these advances, traditional observations of Type Ia supernova host galaxies, progenitors, light curves, and remnants have been unable to accurately and precisely quantify the relative contributions of each of the progenitor systems and explosion mechanisms described above to the population of thermonuclear events observed as Type Ia supernovae (e.g., Maoz et al. 2014). A more accurate and precise understanding of the progenitor systems and explosion mechanisms responsible for Type Ia supernovae would be beneficial for numerous areas of astrophysics from cosmology to galaxy formation to galactic chemical evolution (e.g., Phillips 1993; Riess et al. 1998; Perlmutter et al. 1999; Kobayashi et al. 2020a, 2020b). In this article, we use published nucleosynthetic yields for thermonuclear explosions that are prolific producers of iron to identify a region of elemental abundance space consistent with those yields but rarely observed in metal-poor stars. We label stars in this elemental abundance space “iron-rich metal-poor” (IRMP) and identify three such stars: BD +80°245, HE 0533–5340, and SMSS J034249.53–284216.0. We use a state-of-the-art methodology to homogeneously infer elemental abundances for these stars and compare those abundances to published nucleosynthetic yields to identify the progenitor systems and/or explosion mechanism most consistent with those abundances. We describe in Section 2 the construction of our sample. We then infer stellar parameters for our sample based on high-resolution optical spectra and all available astrometric and photometric data in Section 3. We derive the individual elemental abundances in Section 4. We identify the progenitor system and/or explosion mechanism most consistent with our elemental abundances and the implications of those results in Section 5. We conclude by summarizing our findings in Section 6.

2. Sample Definition

We seek to identify metal-poor stars with $[\text{Fe}/\text{H}] < -1$ formed in regions dominated by thermonuclear nucleosynthesis. We first searched the literature for tables of stable nucleosynthetic yields produced by thermonuclear explosions from any progenitor system and explosion mechanism.⁶ Because models of galactic chemical evolution require thermonuclear explosions to be prolific producers of iron, we only use models that produce $M_{\text{Fe}} \geq 0.1 M_{\odot}$ to define the abundance space dominated by thermonuclear nucleosynthesis. We transform yields in mass to yields in abundance ratio $[\text{X}/\text{Fe}]$ assuming Asplund et al. (2021) solar abundances and plot the results in Figure 1. While in our yield compilation the variance in stable nucleosynthesis can be large, there are commonalities. We find that thermonuclear explosion models that yield $M_{\text{Fe}} \geq 0.1 M_{\odot}$ always produce $[\text{C}, \text{N}, \text{O}, \text{F}, \text{Ne}, \text{Na}, \text{Mg}, \text{Al}, \text{Cl}, \text{K}, \text{Co}, \text{Cu}, \text{Zn}/\text{Fe}] < 0$. Carbon can be synthesized in asymptotic giant branch (AGB) stars, transferred to binary companions, and then transmuted to nitrogen. An IRMP star definition that depends on carbon and nitrogen could therefore fail to identify stars formed in regions dominated by thermonuclear nucleosynthesis subsequently impacted by mass transfer from an AGB star companion. We therefore propose a useful working definition for IRMP stars robust to mass

⁶ The yields in our compilation come from Seitzzahl et al. (2013, 2016), Fink et al. (2014), Ohlmann et al. (2014), Kromer et al. (2015), Papish & Perets (2016), Leung & Nomoto (2018, 2020a, 2020b), Nomoto & Leung (2018), Bravo et al. (2019), Boos et al. (2021), Gronow et al. (2021a, 2021b), and Neopane et al. (2022).

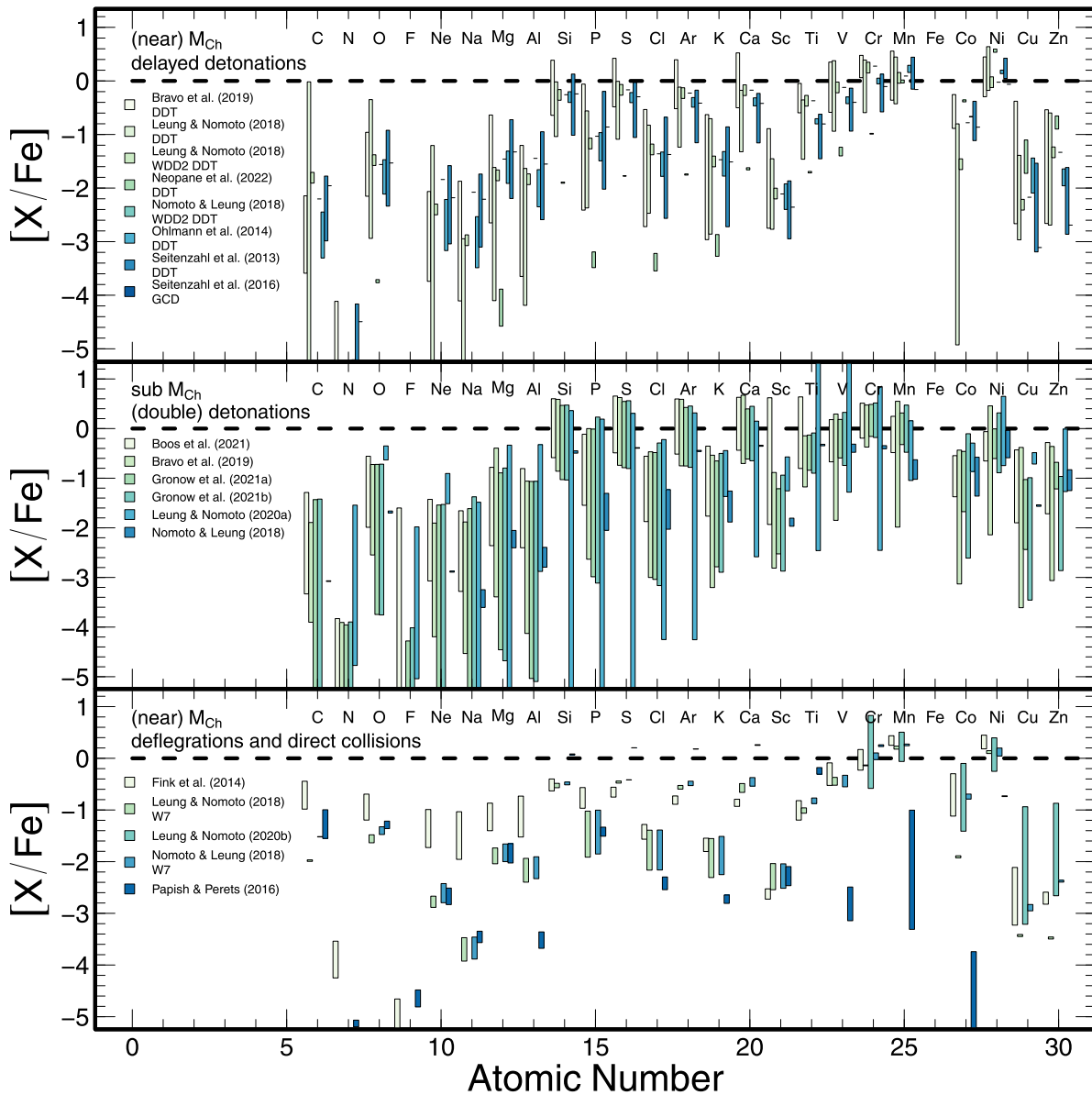


Figure 1. Predicted stable nucleosynthetic yields for thermonuclear explosions that produce $M_{\text{Fe}} \geq 0.1 M_{\odot}$ with varying progenitor systems and explosion mechanisms. Each rectangle represents the full range of predicted elemental abundances after marginalizing over the parameters that define each progenitor system and explosion mechanism. Top: predicted stable elemental abundances produced by delayed detonations. Middle: predicted stable elemental abundances produced by double detonations. Bottom: predicted stable elemental abundances produced by deflagrations and direct collisions. Regardless of the progenitor system or explosion mechanism, relative to iron the elemental abundances of carbon, nitrogen, oxygen, fluorine, neon, sodium, magnesium, aluminum, chlorine, potassium, cobalt, copper, and zinc are always subsolar. From this list, we use in our IRMP star selection sodium, magnesium, and cobalt because those abundances are usually straightforward to infer in the photospheres of metal-poor giants.

transfer $[O, F, Ne, Na, Mg, Al, Cl, K, Co, Cu, Zn/Fe] < 0$. Of these elements, sodium, magnesium, and cobalt are most readily observable in the photospheres of metal-poor giants, and we focus our attention on stars with published $[Na, Mg, Co/Fe] < 0$. The requirement $[Na, Mg/Fe] < 0$ tends to exclude stars enriched by ordinary core-collapse supernovae, while the requirement $[Co/Fe] < 0$ should exclude stars enriched by energetic explosions like hypernovae (e.g., Kobayashi et al. 2020a).

We next searched the Stellar Abundances for Galactic Archaeology (SAGA) database (Suda et al. 2008, 2011; Yamada et al. 2013; Suda et al. 2017) for giant stars with $[Fe/H] < -1$ and $[Na, Mg, Co/Fe] < 0$. We identified four candidate IRMP giants: BD +80°0245, HD 6833, HE

0533–5340, and SMSS J034249.53–284216.0. The photospheric stellar parameters and elemental abundances recorded in SAGA have been inhomogeneously derived, and that makes it difficult to draw robust conclusions from those archival data alone. Consequently, we chose to homogeneously analyze archival high-resolution, high signal-to-noise ratio (S/N) optical spectra ourselves using the state-of-the-art methodology described in Reggiani et al. (2020, 2021, 2022a, 2022b) and Sections 3 and 4.

The uncommon elemental abundances of BD +80°245 were first noted by Carney et al. (1997). Its elemental abundances have been inferred many times since, most recently by Roederer et al. (2014) based on a spectrum collected with the Tull Spectrograph on the 2.7 m Harlan J. Smith Telescope at

Table 1
Observation Log

Designation	R.A. (h:m:s)	Decl. (d:m:s)	UT Date	Telescope/ Instrument	Exposure Time (s)	S/N 4500 Å	S/N 6500 Å
BD +80°245	08:11:06.24	+79:54:29.56	2009 May 06	McDonald-Smith/Tull	7200	70	115
HE 0533–5340	05:34:54.10	–53:38:24.00	2003 Nov 01	Magellan/MIKE	9800	60	100
SMSS J034249.53–284216.0	03:42:49.53	–28:42:15.99	2013 Jan 07	Magellan/MIKE	2000	45	100

McDonald Observatory (Tull et al. 1995). Ian Roederer kindly provided us with the reduced, continuum-normalized spectrum of BD +80°245. The discovery of HE 0533–5340 was reported in Cohen et al. (2013) based on a spectrum collected with the Magellan Inamori Kyocera Echelle (MIKE) spectrograph on the Magellan Clay Telescope at Las Campanas Observatory (Bernstein et al. 2003; Shectman & Johns 2003). Ian Thompson kindly provided us with the reduced spectrum of HE 0533–5340. The discovery of SMSS J034249.53–284216.0 was reported in Jacobson et al. (2015) based on a Magellan/MIKE spectrum. Heather Jacobson kindly provided us with the reduced spectrum of SMSS J034249.53–284216.0. The spectra of both HE 0533–5340 and SMSS J034249.53–284216.0 were reduced using the `CarPy`⁷ software package (Kelson et al. 2000; Kelson 2003; Kelson et al. 2014), and we continuum-normalized those spectra using Spectroscopy Made Harder (`smhr`; Casey 2014).⁸ We report in Table 1 the properties of the spectra we analyze as part of the study described in this article.

The importance of homogeneous analyses using the state-of-the-art methodology described in Reggiani et al. (2020, 2021, 2022a, 2022b) for the realization of precise and accurate stellar parameters and elemental abundances is illustrated by the case of HD 6833. The elemental abundances of HD 6833 have been reported by many authors, and we analyzed an archival spectrum collected with High Resolution Echelle Spectrometer (HIRES) on the Keck I Telescope at the Maunakea Observatories that we downloaded from the Keck Observatory Archive (Vogt et al. 1994). We subsequently found that the priority photospheric stellar parameters recorded in SAGA for HD 6833 from Mishenina et al. (2017) were inaccurate, and we dropped it from our sample because it does not meet our criteria for IRMP stars.

3. Stellar Properties

3.1. Stellar Orbits

We calculate Galactic orbits for the stars in our sample using `Gala`⁹ (Price-Whelan 2017; Price-Whelan et al. 2020). We first sample 1000 Monte Carlo realizations from the Gaia Data Release 3 (DR3) astrometric solutions for each star using the distance posterior described below, taking full account of the covariances between position, parallax, and proper motion (Fabricius et al. 2021; Gaia Collaboration et al. 2021; Lindegren et al. 2021a, 2021b; Torra et al. 2021). We used the radial velocities we measured from the spectra described in Section 2 and assume no covariance between our measured radial velocity and the Gaia DR3 astrometric solution. We use each Monte Carlo realization as an orbital initial condition and integrate an orbit forward in time for 10 Gyr in a Milky Way

–like potential. We adopted the `MWPotential2014` described by Bovy (2015). In that model, the bulge is parameterized as a power-law density profile that is exponentially cut off at 1.9 kpc with a power-law exponent of -1.8 . The disk is represented by a Miyamoto–Nagai potential with a radial scale length of 3 kpc and a vertical scale height of 280 pc (Miyamoto & Nagai 1975). The halo is modeled as a Navarro–Frenk–White halo with a scale length of 16 kpc (Navarro et al. 1996). We set the solar distance to the Galactic center to $R_0 = 8.122$ kpc, the circular velocity at the Sun to $V_0 = 238$ km s^{-1} , the height of the Sun above the plane to $z_0 = 25$ pc, and the solar motion with respect to the local standard of rest to $(U_\odot, V_\odot, W_\odot) = (10.0, 11.0, 7.0)$ km s^{-1} (Jurić et al. 2008; Bland-Hawthorn & Gerhard 2016; Gravity Collaboration et al. 2018). We report the resulting orbital parameters in Table 2. All three stars are on ordinary inner-halo-like orbits with no obvious evidence that they were formed in accreted and tidally disrupted dwarf galaxies.

3.2. Fundamental and Photospheric Stellar Parameters

We derive photospheric and fundamental stellar parameters for the stars in our sample using the algorithm described in Reggiani et al. (2020, 2021, 2022a, 2022b) that makes use of both the classical spectroscopy-only approach¹⁰ and isochrones to infer accurate, precise, and self-consistent photospheric stellar parameters. Isochrones are especially useful for effective temperature T_{eff} inferences in this case, as high-quality multiwavelength photometric data from the ultraviolet to the mid-infrared are available from the Galaxy Evolution Explorer (GALEX), the SkyMapper Southern Survey (SMSS), Gaia, the Two Micron All Sky Survey (2MASS), and the Wide-field Infrared Survey Explorer (WISE). Similarly, the Gaia DR3 parallax-based distances to the stars in our sample make the calculation of surface gravity $\log g$ via isochrones straightforward. With both T_{eff} and $\log g$ available via isochrones, the equivalent widths of iron lines can be used to self-consistently determine metallicity $[\text{Fe}/\text{H}]$ and microturbulence ξ by minimizing the dependence of individual line-based iron abundance inferences on reduced equivalent width. The microturbulence values inferred in this way can then be confirmed using empirical relations (e.g., Kirby et al. 2011a).

The inputs to our photospheric and fundamental stellar parameter inference include the equivalent widths of Fe I and Fe II atomic absorption lines, multiwavelength photometry, a Gaia parallax, and an extinction estimate. Using atomic absorption-line data from Ji et al. (2020) based on the `linemake` code¹¹ (Snedden et al. 2009, 2016; Placco et al. 2021) maintained by Vinicius Placco and Ian Roederer, we first

⁷ <http://code.obs.carnegiescience.edu/mike>

⁸ <https://github.com/andycasey/smhr/tree/py38-mpl313>

⁹ <http://gala.adrian.pw/en/latest/>

¹⁰ The classical spectroscopy-only approach to photospheric stellar parameter estimation involves simultaneously minimizing the difference between Fe I- and Fe II-based abundances, as well as their dependencies on excitation potential and reduced equivalent width.

¹¹ <https://github.com/vmplacco/linemake>

Table 2
Stellar Properties and Adopted Parameters

Property	BD +80°245 1139085117140997120	HE 0533–5340 4768665767426450304	SMSS J034249.53–284216.0 5080395975535412224	Units
Astrometric properties:				
Gaia DR3 parallax π	4.312 ± 0.012	0.062 ± 0.020	0.095 ± 0.016	mas
Gaia DR3 proper motion $\mu_{\alpha} \cos \delta$	136.699 ± 0.0132	6.025 ± 0.026	2.024 ± 0.011	mas yr ⁻¹
Gaia DR3 proper motion μ_{δ}	-367.492 ± 0.012	2.756 ± 0.031	-1.058 ± 0.015	mas yr ⁻¹
Photometric properties:				
GALEX NUV	...	20.402 ± 0.099	...	AB mag
SkyMapper u	...	16.926 ± 0.041	16.357 ± 0.035	AB mag
SkyMapper v	...	16.444 ± 0.019	...	AB mag
SkyMapper g	...	15.309 ± 0.013	14.645 ± 0.011	AB mag
SkyMapper r	...	14.890 ± 0.005	14.270 ± 0.008	AB mag
SkyMapper i	13.950 ± 0.006	AB mag
SkyMapper z	...	14.428 ± 0.008	...	AB mag
Gaia DR2 G	9.803 ± 0.002	14.860 ± 0.002	14.243 ± 0.002	Vega mag
2MASS J	8.711 ± 0.039	13.416 ± 0.028	12.837 ± 0.024	Vega mag
2MASS H	8.333 ± 0.038	12.894 ± 0.024	12.307 ± 0.024	Vega mag
2MASS K_s	8.261 ± 0.026	12.811 ± 0.029	12.224 ± 0.026	Vega mag
WISE W1	8.210 ± 0.023	12.761 ± 0.023	12.168 ± 0.023	Vega mag
WISE W2	8.244 ± 0.021	12.754 ± 0.022	12.182 ± 0.022	Vega mag
Stellar properties:				
Luminosity L_*	5 ± 1	143^{+2}_{-5}	114^{+5}_{-7}	L_{\odot}
Radius R_*	2 ± 1	15 ± 1	14 ± 1	R_{\odot}
Distance d_{iso}	0.2 ± 0.1	$11.2^{+0.1}_{-0.2}$	$7.8^{+0.2}_{-0.3}$	kpc
Mass M_{\odot}	$0.79^{+0.02}_{-0.01}$	$0.82^{+0.03}_{-0.02}$	$0.86^{+0.09}_{-0.06}$	M_{\odot}
Age τ	$12.3^{+0.7}_{-0.9}$	$12.3^{+0.9}_{-1.4}$	$9.2^{+2.6}_{-2.5}$	Gyr
Extinction A_V	$0.090^{+0.038}_{-0.028}$	$0.219^{+0.015}_{-0.014}$	$0.138^{+0.029}_{-0.027}$	mag
Effective temperature T_{eff}	5696^{+47}_{-36}	5031^{+11}_{-9}	5017^{+26}_{-23}	K
Surface gravity $\log g$	3.57 ± 0.01	1.94 ± 0.02	2.08 ± 0.04	cm s ⁻²
Metallicity [Fe/H]	-1.73 ± 0.11	-2.44 ± 0.15	-1.97 ± 0.17	
Microturbulence ξ	1.31 ± 0.10	1.68 ± 0.10	1.65 ± 0.10	km s ⁻¹
Orbital properties:				
Radial velocity v_r	5.0 ± 0.2	147.2 ± 1.5	156.7 ± 3.5	km s ⁻¹
Total Galactic velocity v	$185.5^{+114.5}_{-62.0}$	$211.6^{+28.0}_{-24.3}$	$196.4^{+100.4}_{-56.6}$	km s ⁻¹
Pericenter R_{peri}	$5.28^{+0.04}_{-0.04}$	$11.61^{+3.19}_{-5.71}$	$5.43^{+0.23}_{-0.29}$	kpc
Apocenter R_{apo}	$15.83^{+0.21}_{-0.20}$	$15.66^{+14.50}_{-3.41}$	$13.56^{+0.95}_{-0.91}$	kpc
Eccentricity e	0.5 ± 0.1	$0.26^{+0.19}_{-0.10}$	$0.43^{+0.05}_{-0.05}$	
Maximum distance from Galactic plane z_{max}	$9.48^{+0.08}_{-0.08}$	$12.61^{+8.18}_{-4.83}$	$5.25^{+0.34}_{-0.35}$	kpc
Angular momentum L_z	0.7 ± 0.1	-1.1 ± 0.10	-1.4 ± 0.1	kpc km s ⁻¹
Specific orbital energy E_{tot}	-1.2 ± 0.1	-1.1 ± 0.1	-1.3 ± 0.1	$10^5 \text{ km}^2 \text{ s}^{-2}$

Note. We report random uncertainties derived under the unlikely assumption that the MIST isochrone grid perfectly reproduces all stellar properties. There are almost certainly larger systematic uncertainties that we have not investigated, though the excellent agreement between our analysis and previous results for the three stars in our sample indicates that any systematic uncertainties in our analysis cannot be too large.

measure equivalent widths of atomic absorption lines by fitting Gaussian profiles with `smhr` to a continuum-normalized spectrum. We gather

1. NUV photometry and their uncertainties from GALEX (Bianchi et al. 2017);
2. u , v , g , r , i , and z photometry and their uncertainties from SMSS DR2 (Onken et al. 2019);
3. G photometry and their uncertainties from Gaia DR2 (Gaia Collaboration et al. 2016; Arenou et al. 2018; Evans et al. 2018; Gaia Collaboration et al. 2018; Hambly et al. 2018; Riello et al. 2018);
4. J , H , and K_s photometry and their uncertainties from the 2MASS Point Source Catalog (Skrutskie et al. 2006); and

5. W1 and W2 photometry and their uncertainties from the WISE AllWISE data release (Wright et al. 2010; Mainzer et al. 2011).

We use Gaia DR3 parallaxes and their uncertainties (Lindgren et al. 2021a, 2021b; Fabricius et al. 2021; Gaia Collaboration et al. 2021; Torra et al. 2021), as well as extinction A_V inferences. For BD +80°245, HE 0533–5340, and SMSS J034249.53–284216.0 we take A_V from the three-dimensional (3D) Stilism reddening maps (Lallement et al. 2014; Capitanio et al. 2017; Lallement et al. 2018), the Schlegel et al. (1998) dust map as updated by Schlafly & Finkbeiner (2011), and the 3D Bayestar19 dust map (Green et al. 2019), respectively.

We assume Asplund et al. (2021) solar abundances and use these inputs to infer photospheric and fundamental stellar parameters using the following steps:

1. We use 1D plane-parallel solar-composition ATLAS9 model atmospheres (Castelli & Kurucz 2004), the 2019 version of the MOOG radiative transfer code (Snedden 1973), and the q^2 MOOG wrapper¹² (Ramírez et al. 2014) to derive an initial set of photospheric stellar parameters T_{eff} , $\log g$, $[\text{Fe}/\text{H}]$, and ξ using the classical spectroscopy-only approach.
2. We then use the `isochrones` package¹³ (Morton 2015) to fit the MESA Isochrones and Stellar Tracks (MIST; Paxton et al. 2011, 2013, 2015; Choi et al. 2016; Dotter 2016; Paxton et al. 2018, 2019; Jermyn et al. 2023) library to our photospheric stellar parameters, as well as our input multiwavelength photometry, parallax, and extinction data using `MultiNest`¹⁴ (Feroz & Hobson 2008; Feroz et al. 2009, 2019) via `PyMultiNest` (Buchner et al. 2014). We restricted the MIST library to extinctions between $A_V=0$ mag and the maximum suggested extinction for a particular star plus 0.1 mag. This produces a new set of photospheric and fundamental stellar parameter posteriors that are both self-consistent and physically consistent with stellar evolution.
3. We next impose the posterior-median T_{eff} and $\log g$ inferred in step 2 on our grid of model atmospheres and minimize the dependence of individual line-based iron abundance inferences on reduced equivalent width to derive model atmosphere $[\text{Fe}/\text{H}]_{\text{atmo}}$ and a new set of ξ values consistent with our measured Fe I and Fe II equivalent widths and our `isochrones`-inferred T_{eff} and $\log g$.
4. We then use the model atmosphere selected in step 3 to calculate $[\text{Fe}/\text{H}]$ as the average of all $n_{\text{Fe}} = n_{\text{Fe I}} + n_{\text{Fe II}}$ equivalent-width-based iron abundance inferences for individual Fe I and Fe II lines. We take the uncertainty of our $[\text{Fe}/\text{H}]$ inference $\sigma_{[\text{Fe}/\text{H}]}$ as the standard deviation of the individual line-based abundance inferences $\sigma_{[\text{Fe}/\text{H}]}$ divided by $\sqrt{n_{\text{Fe}}}$.
5. We next check whether the $[\text{Fe}/\text{H}]$ inferred in step 4 agrees to two decimal places with $[\text{Fe}/\text{H}]_{\text{atmo}}$. If so, we proceed to step 6. If not, we replace $[\text{Fe}/\text{H}]_{\text{atmo}}$ with $[\text{Fe}/\text{H}]$ and repeat steps 3–5 until agreement is achieved.
6. We then repeat steps 2–5 until the metallicities inferred from both the `isochrones` analysis and the reduced equivalent width balance approach are consistent within their uncertainties (typically a few iterations).

We use a Monte Carlo simulation to derive the final values and uncertainties in our adopted $[\text{Fe}/\text{H}]$ and ξ values due to the uncertainties in our adopted T_{eff} and $\log g$.

1. We randomly sample a self-consistent pair of T_{eff} and $\log g$ from our converged `isochrones` posteriors described above and calculate the values of $[\text{Fe}/\text{H}]_{\text{atmo}}$ and ξ that produce the best reduced equivalent width balance given our Fe I and Fe II equivalent width measurements.

2. We use the model atmosphere selected in step 1 to calculate the average of all $n_{\text{Fe}} = n_{\text{Fe I}} + n_{\text{Fe II}}$ individual equivalent-width-based iron abundance inferences and save the resulting metallicity of each iteration.
3. We repeat steps 1 and 2 a total of 200 times and adopt as our final photospheric stellar parameters the (16th, 50th, 84th) percentiles of the 200 self-consistent sets of T_{eff} , $\log g$, $[\text{Fe}/\text{H}]$, and ξ produced in this way.

We find good agreement between these photospheric stellar parameters derived from our Monte Carlo simulation and those resulting from a single iteration of reduced equivalent width balance using the median T_{eff} and $\log g$ from the posteriors produced by our converged analysis. We report our adopted photospheric and fundamental stellar parameters in Table 2. All of the uncertainties quoted in Table 2 include random uncertainties only. That is, they are uncertainties derived under the unlikely assumption that the MIST isochrone grid we use in our analyses perfectly reproduces all stellar properties.

To evaluate the impact of any possible systematic uncertainties resulting from our analysis, we compare the photospheric stellar parameters we infer for the stars in our sample with those reported by other groups for the same stars. Photospheric stellar parameters for BD +80°245 based on high-resolution optical spectra using modern analysis techniques have been presented by many authors.

1. Carney et al. (1997) found $T_{\text{eff}} = 5400 \pm 100$ K, $\log g = 3.2 \pm 0.14$, $[\text{Fe}/\text{H}] = -1.86 \pm 0.05$, and $\xi = 1.5 \pm 0.2$ km s⁻¹;
2. Fulbright (2000) found $T_{\text{eff}} = 5225 \pm 40$ K, $\log g = 3.0 \pm 0.06$, $[\text{Fe}/\text{H}] = -1.90 \pm 0.08$, and $\xi = 1.35 \pm 0.11$ km s⁻¹;
3. Stephens & Boesgaard (2002) found $T_{\text{eff}} = 5569 \pm 121$ K, $\log g = 3.47 \pm 0.46$, $[\text{Fe}/\text{H}] = -1.76 \pm 0.09$, and $\xi = 1.56 \pm 0.09$ km s⁻¹;
4. Ivans et al. (2003) found $T_{\text{eff}} = 5225$ K, $\log g = 3.00$, $[\text{Fe}/\text{H}] = -2.07$, and $\xi = 1.25$ km s⁻¹;
5. Zhang & Zhao (2005) found $T_{\text{eff}} = 5446 \pm 100$ K, $\log g = 3.31 \pm 0.20$, $[\text{Fe}/\text{H}] = -1.72 \pm 0.10$, and $\xi = 1.90 \pm 0.50$ km s⁻¹; and
6. Roederer et al. (2014) found $T_{\text{eff}} = 5360 \pm 34$ K, $\log g = 3.15 \pm 0.22$, $[\text{M}/\text{H}] = -2.01 \pm 0.07$, and $\xi = 1.20 \pm 0.06$ km s⁻¹.

HE 0533–5340 was initially studied by Cohen et al. (2013) in the paper announcing its discovery, and those authors found $T_{\text{eff}} = 4937 \pm 100$ K, $\log g = 1.80 \pm 0.25$, $[\text{Fe}/\text{H}] = -2.67 \pm 0.20$, and $\xi = 2.1 \pm 0.2$ km s⁻¹. SMSS J034249.53–284216.0 was initially studied by Jacobson et al. (2015) in the paper announcing its discovery, and those authors found $T_{\text{eff}} = 4828 \pm 100$ K, $\log g = 1.91 \pm 0.3$, $[\text{Fe}/\text{H}] = -2.33 \pm 0.14$, and $\xi = 1.95 \pm 0.2$ km s⁻¹. In general, our photospheric stellar parameters are consistent with those previously inferred for the same stars. These previous analyses mostly used the classical spectroscopy-only approach in the pre-Gaia era, though, and we attribute any differences between our and previous inferences to the well-known tendency of spectroscopy-only inferences to obtain cooler temperatures and lower surface gravities than photometry- and parallax-informed methods (e.g., Korn et al. 2003; Frebel et al. 2013; Mucciarelli & Bonifacio 2020).

¹² <https://github.com/astroChasqui/q2>

¹³ <https://github.com/timothydmorton/isochrones>

¹⁴ <https://ccpforge.cse.rl.ac.uk/gf/project/multinest/>

Table 3
Atomic Data, Equivalent Width Measurements, and Individual Line-based Abundance Inferences

Star	Wavelength (Å)	Species	Excitation Potential (eV)	log(<i>gf</i>)	EW (mÅ)	log(ϵ) (X)
BD +80°0245	5889.951	Na I	0.000	0.108	160.71	4.402
HE 0533–5340	5889.951	Na I	0.000	0.108	110.31	3.174
SMSS J034249.53–284216.0	5889.951	Na I	0.000	0.108	154.12	3.865
BD +80°0245	3986.753	Mg I	4.346	–1.060	29.85	5.659
BD +80°0245	4057.505	Mg I	4.346	–0.900	36.30	5.622
BD +80°0245	4571.096	Mg I	0.000	–5.623	20.28	5.732
HE 0533–5340	4057.505	Mg I	4.346	–0.900	15.70	4.877
HE 0533–5340	4167.271	Mg I	4.346	–0.745	27.07	5.011
HE 0533–5340	4571.096	Mg I	0.000	–5.623	16.56	4.765
SMSS J034249.53–284216.0	3986.753	Mg I	4.346	–1.060	17.88	5.092
SMSS J034249.53–284216.0	4057.505	Mg I	4.346	–0.900	41.11	5.419
SMSS J034249.53–284216.0	4167.271	Mg I	4.346	–0.745	53.94	5.473

Notes. This table is published in its entirety in the machine-readable format. A portion is shown here for guidance regarding its form and content.

(This table is available in its entirety in machine-readable form.)

As an additional check, we infer T_{eff} using the `colte` code¹⁵ (Casagrande et al. 2021) that estimates T_{eff} using a combination of color– T_{eff} relations obtained by implementing the InfraRed Flux Method for Gaia and 2MASS photometry. As required by `colte`, we used Gaia DR3 G , G_{BP} , and G_{RP} plus 2MASS J , H , and K_s photometry as input. Using this approach, we find $T_{\text{eff}} = 5601 \pm 61$ K for BD +80°0245, $T_{\text{eff}} = 5003 \pm 59$ K for HE 0533–5340, and $T_{\text{eff}} = 4943 \pm 53$ K for SMSS J034249.53–285216.0. These IRFM-based temperatures are consistent with our adopted values. We are therefore confident that any systematic uncertainties arising from our methodology should be small.

4. Elemental Abundances

To infer the elemental abundances of several α -, light odd-Z, iron-peak, and neutron-capture elements, we first measure the equivalent widths of atomic absorption lines of O I, Na I, Mg I, Al I, Si I, Ca I, Sc II, Ti I, Ti II, Cr I, Cr II, Mn I, Fe I, Fe II, Ni I, Zn I, Sr II, Y II, and Ba II in our continuum-normalized spectra by fitting Gaussian or Voigt profiles as appropriate with `smhr`. We use atomic absorption-line data from Ji et al. (2020) based on the `linemake` code¹⁶ (Snedden et al. 2009, 2016; Placco et al. 2021). We measure an equivalent width for every absorption line in our line list that could be recognized, taking into consideration the quality of the spectrum in the vicinity of a line and the availability of alternative transitions of the same species. We assume Asplund et al. (2021) solar abundances and local thermodynamic equilibrium (LTE) and use the 1D plane-parallel solar-composition ATLAS9 model atmospheres and the 2019 version of MOOG to infer elemental abundances based on each equivalent width measurement. We report our adopted atomic data, equivalent width measurements, and individual line-based abundance inferences in Table 3.

We use spectral synthesis to infer the abundances of elements that are difficult or impossible to measure in our spectra using equivalent widths. Cobalt lines in our spectra are too weak for the equivalent width approach, so we inferred cobalt abundances using up to six Co I lines at 3894, 3995, 4020, 4110, 4118, and 4121 Å. We also use spectral synthesis

to infer europium abundances using up to three Eu II lines at 4129, 4435, and 4522 Å. We account for the effects of hyperfine and/or isotopic splitting on lines of Sc II, Mn I, Co I, Y II, Ba II, and Eu II using data from Kurucz¹⁷ supplemented by data from McWilliam (1998) and Klose et al. (2002) for barium. We present our adopted mean elemental abundances and uncertainties in Table 4. We define the uncertainty in the abundance ratio $\sigma_{[\text{X}/\text{H}]}$ as the standard deviation of the individual line-based abundance inferences $\sigma_{[\text{X}/\text{H}]}$ divided by $\sqrt{n_{\text{X}}}$. We define the uncertainty $\sigma_{[\text{X}/\text{Fe}]}$ as the square root of the sum of squares of $\sigma_{[\text{X}/\text{H}]}$ and $\sigma_{[\text{Fe}/\text{H}]}$.

4.1. α -elements

Oxygen, magnesium, silicon, calcium, and titanium are often referred to as α -elements. Oxygen is produced in helium and neon burning (^{16}O), as well as the CNO tri-cycle in hydrogen shell burning (^{17}O) and through α -capture by ^{14}N during helium shell burning (^{18}O) (Woosley & Weaver 1995). Magnesium, silicon, and calcium are formed via similar nucleosynthetic channels. Magnesium is mainly synthesized by carbon burning in core-collapse supernovae, and at solar metallicities thermonuclear events provide at least an order of magnitude less. Silicon is mostly a product of oxygen burning and is itself the most abundant product of oxygen burning. At solar metallicity core-collapse and thermonuclear supernovae contribute equally to silicon production. Calcium is the product of both hydrostatic and explosive oxygen and silicon burning. At solar metallicity it is mostly produced in core-collapse supernovae. Even though titanium forms either in the α -rich freezeout of shock-decomposed nuclei during core-collapse supernovae or in explosive ^4He fusion in the envelopes of CO white dwarfs during thermonuclear explosions (e.g., Woosley & Weaver 1994; Livne & Arnett 1995), it is often considered alongside the true α -elements because of their similar chemical abundances (Clayton 2003). At solar metallicity both core-collapse and thermonuclear explosions are important sources of titanium. Magnesium, silicon, calcium, and titanium abundance inferences based on the lines we use are not strongly affected by departures from the assumptions of LTE. Nevertheless, we correct magnesium and silicon abundances for departures from

¹⁵ <https://github.com/casaluca/colte>

¹⁶ <https://github.com/vmplacco/linemake>

¹⁷ <http://kurucz.harvard.edu/linelists.html>

Table 4
Elemental Abundances

Species	n	$\log(\epsilon_X)$	[X/Fe]	$\sigma_{[X/Fe]}$	n	$\log(\epsilon_X)$	[X/Fe]	$\sigma_{[X/Fe]}$	n	$\log(\epsilon_X)$	[X/Fe]	$\sigma_{[X/Fe]}$
BD +80°0245				HE 0533–5340				SMSS J034249.53–284216.0				
O I	2	7.325	0.365	0.273
Na I	2	4.438	−0.052	0.077	2	3.174	−0.604	0.045	2	3.788	−0.463	0.105
Na I _{NLTE}	2	3.963	−0.527	...	2	2.901	−0.877	...	2	3.325	−0.926	...
Mg I	6	5.615	−0.205	0.059	7	4.855	−0.253	0.036	7	5.300	−0.281	0.069
Mg I _{NLTE}	1	5.772	−0.095	1	5.429	−0.167	...
Al I	1	3.163	−1.537	0.067	1	2.600	−1.388	0.049	1	3.066	−1.395	0.073
Si I	1	5.759	−0.021	0.052	1	5.546	0.478	0.027	1	5.769	0.228	0.052
Si I _{NLTE}	1	5.803	−0.024	...	1	5.524	0.426	...	1	5.738	0.182	...
Ca I	23	4.306	−0.264	0.046	14	3.753	−0.105	0.041	18	4.154	−0.177	0.068
Sc II	2	0.859	−0.551	0.077	1	−0.014	−0.712	0.014	3	0.696	−0.475	0.225
Ti I	21	3.201	−0.039	0.112	14	2.316	−0.212	0.041	30	2.883	−0.118	0.093
Ti II	29	3.078	−0.162	0.051	32	2.530	0.002	0.055	43	2.934	−0.067	0.067
Cr I	16	3.799	−0.091	0.060	10	2.890	−0.288	0.065	14	3.263	−0.388	0.058
Cr II	5	3.821	−0.069	0.040	2	3.214	0.036	0.202	5	3.362	−0.289	0.042
Mn I	4	3.466	−0.224	0.110	1	3.069	0.091	0.012	2	3.151	−0.300	0.048
Fe I	117	5.739	115	5.026	121	5.480
Fe I _{NLTE}	117	5.874	...	0.092	115	5.053	...	0.113	121	5.543	...	0.148
Fe II	23	5.682	19	4.970	25	5.542
Fe II _{NLTE}	23	5.727	...	0.115	19	4.998	...	0.101	25	5.569	...	0.160
Co I	5	3.230	−0.023	0.100	6	2.250	−0.273	0.150	6	2.620	−0.370	0.150
Ni I	21	4.367	−0.103	0.063	11	3.729	−0.029	0.125	22	4.099	−0.132	0.065
Zn I	2	2.379	−0.451	0.035	1	2.182	−0.409	0.017
Sr II	2	0.293	−0.807	0.228	2	−0.149	−0.537	0.097	2	0.575	−0.286	0.066
Y II	2	−0.385	−0.626	0.212
Ba II	2	−0.887	−1.427	0.057	4	−1.178	−1.006	0.052	4	0.231	−0.070	0.130
Ba II _{NLTE}	1	−1.079	−0.937	...	3	−0.02	−0.336	0.076
Eu II	1	≤ −1.700	≤ −0.533	...	1	≤ −2.410	≤ −0.513	...	1	−1.140	0.290	0.200

the assumptions of LTE (i.e., non-LTE or NLTE) using data from Osorio et al. (2015) and Amarsi & Asplund (2017).

We report in Table 4 the magnesium, silicon, calcium, and titanium abundances we infer for the three IRMP stars in our sample and plot them in Figure 2 along with several comparison samples. While $[Mg/Fe] < 0$ was required for these three IRMP stars by construction, they also have subsolar $[Ca/Fe]$ and $[Ti/Fe]$ abundances. Subsolar $[\alpha/Fe]$ at $[Fe/H] \lesssim -1$ are observed in classical dwarf spheroidal (dSph) galaxies, and Milky Way stars with this property are often attributed to the accretion of now-disrupted dSph galaxies. As is apparent in Figure 2, though, the $[Mg/Fe]$, $[Ca/Fe]$, and $[Ti/Fe]$ abundances we observe in these three IRMP stars are low even for stars at similar metallicities in dSph galaxies. As we will argue in Section 5, while the α -element abundances of these three stars might be attributed to formation in dSph galaxies, the complete set of each IRMP star’s elemental abundances does not support this interpretation.

By themselves the subsolar abundances of $[Ca/Fe]$ and $[Ti/Fe]$ we observe generally disfavor thermonuclear explosions produced by white dwarf collisions or spot- or belt-like double detonations with either especially thin or especially thick helium envelopes. More specifically, subsolar $[Ca/Fe]$ abundances disfavor

1. double-detonation models from Boos et al. (2021) with total masses $M_{\text{tot}} \leq 0.9 M_{\odot}$ and thin helium shells $\rho_{\text{base}} \leq 3 \times 10^5 \text{ g cm}^{-3}$;
2. M_{Ch} -mass DDT models from Bravo et al. (2019) with low densities ahead of the flame at the moment the DDT occurs $\rho_{\text{DDT}} \leq 1.6 \times 10^7 \text{ g cm}^{-3}$ at all metallicities and independent of the uncertain $^{12}\text{C} + ^{16}\text{O}$ reaction rate;

3. sub- M_{Ch} mass detonation models from Bravo et al. (2019) with white dwarf masses $M_{\text{WD}} \leq 0.97 M_{\odot}$ except for the highest-metallicity $M_{\text{WD}} = 0.97 M_{\odot}$ model with $Z = 6.75 \times 10^{-2}$;
4. double-detonation models from Gronow et al. (2021a, 2021b) with initial core masses $M_{\text{c,ini}} \lesssim 0.8 M_{\odot}$ and helium shell masses $M_{\text{c,ini}} \lesssim 0.1 M_{\odot}$, as well as the model with $M_{\text{c,ini}} = 0.905 M_{\odot}$ and the lowest helium shell masses $M_{\text{c,ini}} = 0.026 M_{\odot}$; and
5. white dwarf collisions models from Papish & Perets (2016).

Subsolar $[Ti/Fe]$ abundances disfavor

1. double-detonation models from Boos et al. (2021) with total masses $M_{\text{tot}} = 1.0 M_{\odot}$ and thick helium shells $\rho_{\text{base}} \geq 6 \times 10^5 \text{ g cm}^{-3}$; and
2. double-detonation models from Leung & Nomoto (2020a) with model $M \approx 1 M_{\odot}$, $M_{\text{He}} \approx 0.1 M_{\odot}$, and spot- or belt-like detonations.

4.2. Light Odd-Z Elements

Sodium, aluminum, and scandium are often referred to as light odd- Z elements. Like magnesium, sodium is mostly produced in core-collapse supernovae via carbon burning. Unlike magnesium, the surviving fraction of sodium in supernova ejecta depends on metallicity, so it is treated as a secondary product. Sodium is also a product of hydrogen and helium fusion in thermonuclear explosions, though in smaller quantities than in core-collapse supernovae. Similar to sodium, aluminum is synthesized during carbon fusion in core-collapse supernovae in a secondary reaction that is dependent on the

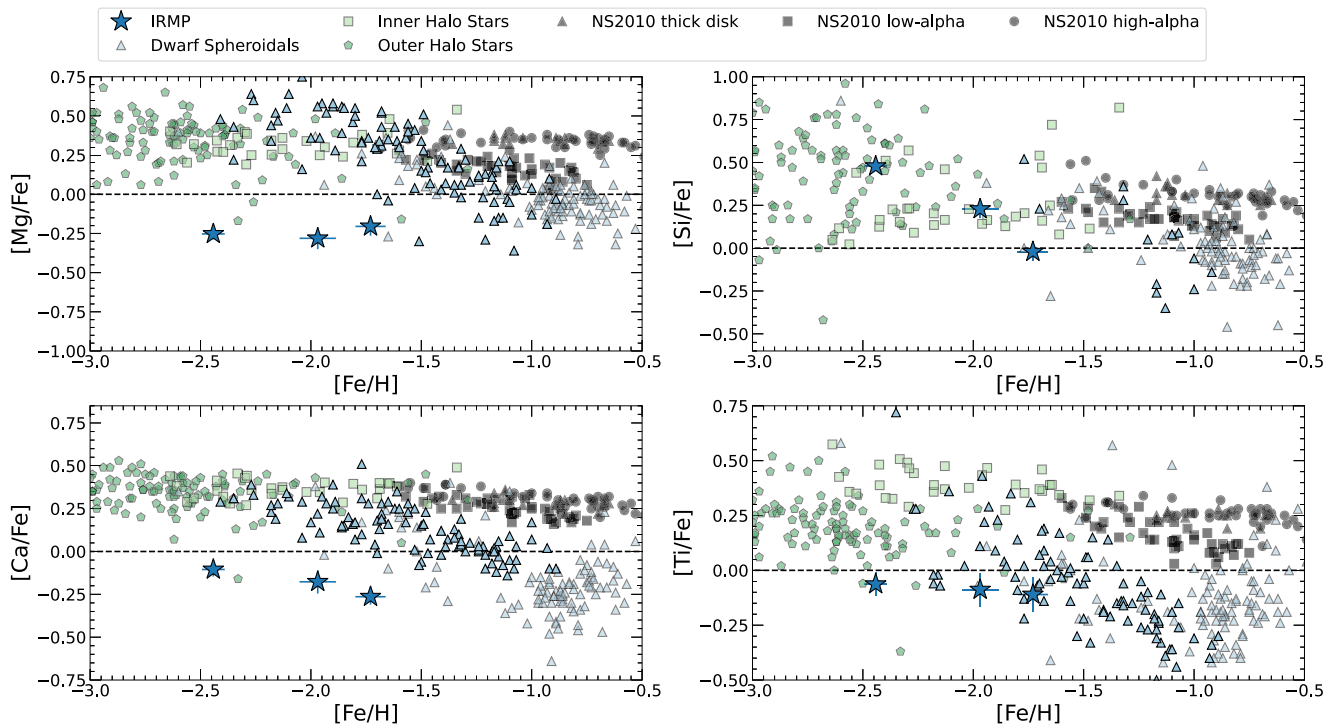


Figure 2. Abundances of titanium and the α -elements magnesium, silicon, and calcium. We plot as dark-blue stars the three IRMP stars in our sample. We plot as black-bordered light-green squares inner-halo metal-poor stars from Reggiani et al. (2017) and H. R. Reggiani et al. (2023, in preparation); as dark-gray triangles, squares, and circles thick-disk, low- α , and high- α stars from Nissen & Schuster (2010), respectively; as black-bordered light-blue triangles stars from the dSph galaxies Carina, Fornax, Sagittarius, and Sculptor (Shetrone et al. 2003; Geisler et al. 2005; Monaco et al. 2005; Letarte et al. 2010; Hill et al. 2019; Skúladóttir et al. 2019); and as dark-green pentagons outer-halo metal-poor stars from Cayrel et al. (2004) and Jacobson et al. (2015). By construction, our three IRMP stars have low $[\text{Mg}/\text{Fe}]$ abundances. Their low $[\text{Ca}/\text{Fe}]$ and $[\text{Ti}/\text{Fe}]$ abundances generally disfavor spot- or belt-like double detonations with either especially thin or especially thick helium envelopes. Direct white dwarf collisions are also disfavored.

amount of ^{22}Ne burned (which in turn depends on the carbon and oxygen content of the star). While sodium and aluminum are mostly produced in core-collapse supernovae, their yields are dependent on metallicity, and consequently their chemical evolution is not as easily interpreted as the chemical evolution of the α -elements. In contrast to sodium and aluminum, scandium is formed both via oxygen burning in core-collapse supernovae and as a product of α -rich freezeout in the shocked region just above the rebounded core (Clayton 2003). Both the exact nucleosynthetic origin and chemical evolution of scandium are hard to precisely identify and interpret because chemical evolution models largely underproduce scandium (e.g., Clayton 2003; Zhao et al. 2016; Prantzos et al. 2018; Kobayashi et al. 2020a).

Sodium and aluminum abundance inferences can be strongly affected by departures from LTE, but scandium abundance inferences based on Sc II lines are not strongly affected (e.g., Zhao et al. 2016). We correct sodium abundances for departures from the assumptions of LTE using the Lind et al. (2011) grid through the INSPECT project.¹⁸

We report in Table 4 the sodium, aluminum, and scandium abundances we infer for the three IRMP stars in our sample and plot them in Figure 3 along with several comparison samples. While $[\text{Na}/\text{Fe}] < 0$ was required for these three IRMP stars by construction, they also have subsolar $[\text{Al}/\text{Fe}]$ and $[\text{Sc}/\text{Fe}]$ abundances. The $[\text{Na}/\text{Fe}]$ and $[\text{Sc}/\text{Fe}]$ abundances of these three IRMP stars are at the lower envelope of the $[\text{Na}/\text{Fe}]$ and $[\text{Sc}/\text{Fe}]$ distributions defined by our comparison samples. We

emphasize that some of our comparison samples' sodium abundances we plot in Figure 3 have not been corrected for departures from the assumptions of LTE that, according to Lind et al. (2011), can be as large -0.5 dex (e.g., Shetrone et al. 2003; Cayrel et al. 2004; Geisler et al. 2005; Monaco et al. 2005; Letarte et al. 2010; Nissen & Schuster 2010). Because corrections for departures from the assumptions of LTE are specific to individual lines, as well as dependent on photospheric parameters and equivalent width/LTE abundance, it would not be advisable to apply them to previously published abundances. Nevertheless, if we did perform that exercise, the sodium abundances we infer for the three stars in our sample would still be at the lower envelope defined by our comparison samples. The observation of subsolar $[\text{Mg}/\text{Fe}]$, $[\text{Ca}/\text{Fe}]$, $[\text{Na}/\text{Fe}]$, and $[\text{Sc}/\text{Fe}]$ abundances in the same star is unusual in both the Milky Way and classical dSph galaxies, suggesting that these three stars we define as IRMP stars do indeed have unusually large amounts of iron given their α -element and light odd- Z element abundances. Consistent with the implications of subsolar $[\text{Ti}/\text{Fe}]$ abundances, subsolar $[\text{Sc}/\text{Fe}]$ abundances generally disfavor thermonuclear explosions produced by double detonations in thick helium envelopes.

4.3. Iron-peak Elements

Chromium, manganese, cobalt, nickel, and zinc are often referred to as iron-peak elements. Iron-peak elements can be formed directly in or as a by-product of explosive silicon burning, either incomplete (chromium and manganese) or complete (cobalt, nickel, and zinc). Their nucleosynthesis mainly takes place in thermonuclear explosions (e.g.,

¹⁸ <http://inspect-stars.com/>

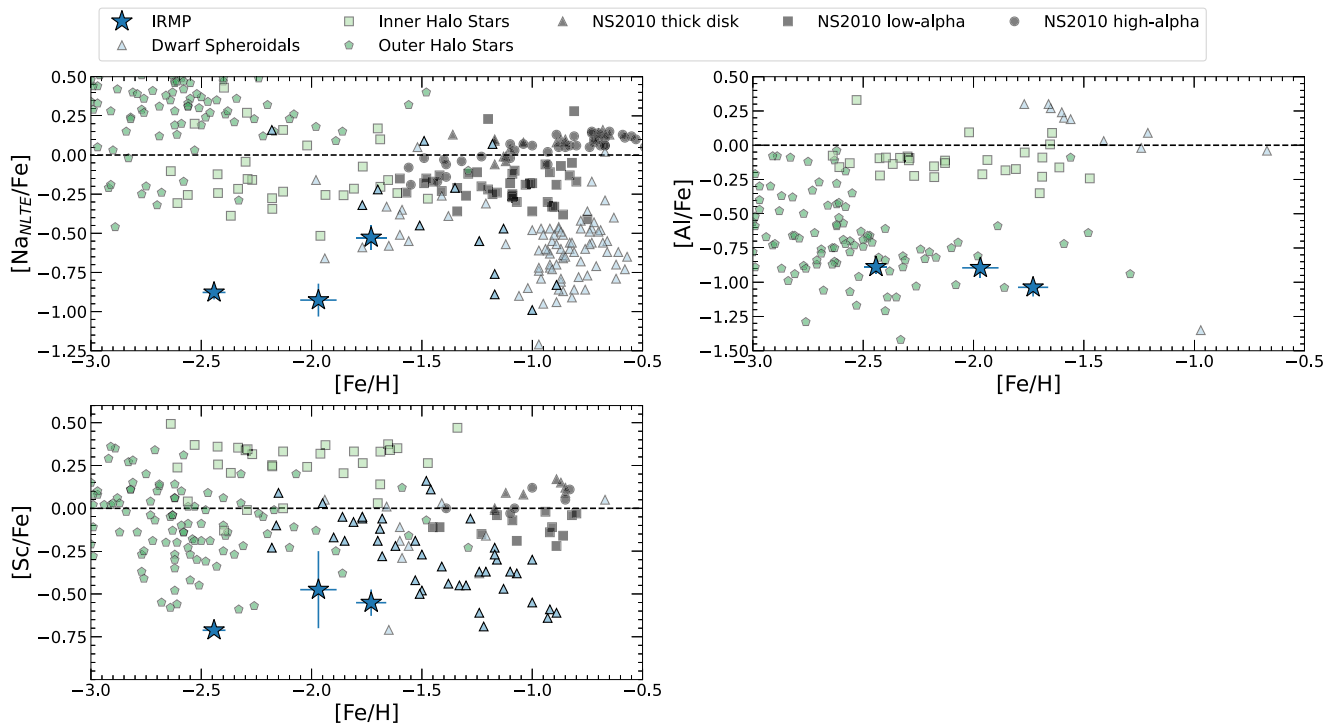


Figure 3. Abundances of the light odd-Z elements sodium, aluminum, and scandium. We plot as dark-blue stars the three IRMP stars in our sample. We plot as black-bordered light-green squares inner-halo metal-poor stars from Reggiani et al. (2017) and H. R. Reggiani et al. (2023, in preparation); as dark-gray triangles, squares, and circles thick-disk, low- α , and high- α stars from Nissen & Schuster (2010), respectively; as black-bordered light-blue triangles stars from the dSph galaxies Carina, Fornax, Sagittarius, and Sculptor (Shetrone et al. 2003; Geisler et al. 2005; Monaco et al. 2005; Letarte et al. 2010; Hill et al. 2019; Skúladóttir et al. 2019); and as dark-green pentagons outer-halo metal-poor stars from Cayrel et al. (2004) and Jacobson et al. (2015). By construction, our three IRMP stars have low $[\text{Na}/\text{Fe}]$ abundances. Consistent with the implications of subsolar $[\text{Ti}/\text{Fe}]$ abundances, subsolar $[\text{Sc}/\text{Fe}]$ abundances generally disfavor double detonations in thick helium envelopes.

Clayton 2003; Grimmett et al. 2020). Cobalt and zinc yields are correlated with the explosion energy of the nucleosynthetic event. In this interpretation, the observed increase in the abundances of $[\text{Co}/\text{Fe}]$ and $[\text{Zn}/\text{Fe}]$ with decreasing $[\text{Fe}/\text{H}]$ in metal-poor stars is evidence of an increased share of iron-peak nucleosynthesis in core-collapse supernovae. Contributions from hypernova events are possible at $[\text{Fe}/\text{H}] \lesssim -3.0$ (e.g., Cayrel et al. 2004; Reggiani et al. 2017; Kobayashi et al. 2020a). While chromium abundance inferences based on Cr I lines are strongly affected by departures from the assumptions of LTE (e.g., Bergemann & Cescutti 2010), we also infer chromium abundances based on Cr II lines that are much less affected by departures from the assumptions of LTE. Manganese, cobalt, nickel, and zinc abundance inferences based on the lines we use are not strongly affected by departures from the assumptions of LTE. We correct iron abundances for departures from the assumptions of LTE using data from Amarsi et al. (2016).

We report in Table 4 the chromium, manganese, cobalt, nickel, and zinc abundances we infer for the three IRMP stars in our sample and plot them in Figure 4 along with several comparison samples. In accord with our comparison samples, we plot in Figure 4 Cr I abundances despite their sensitivity to departures from the assumptions of LTE. The $[\text{Co}/\text{Fe}]$ abundances of our three IRMP stars are all subsolar by construction. The $[\text{Cr}/\text{Fe}]$, $[\text{Ni}/\text{Fe}]$, and $[\text{Zn}/\text{Fe}]$ abundances we infer for our sample are subsolar as well, and our $[\text{Zn}/\text{Fe}]$ inferences for BD +80°245 and SMSS J034249.53–284216.0 are at the lower envelope of the $[\text{Zn}/\text{Fe}]$ distribution defined by our comparison samples. On the other hand, the $[\text{Mn}/\text{Fe}]$

abundances of the three IRMP stars are at the upper envelope of the $[\text{Mn}/\text{Fe}]$ distribution defined by our comparison samples.

Almost all manganese is synthesized in thermonuclear explosions. The high $[\text{Mn}/\text{Fe}]$ abundances we infer for our three IRMP stars relative to our comparison samples support our assertion that IRMP stars formed in environments where the contribution of thermonuclear events to iron-peak nucleosynthesis was above average. Indeed, the manganese abundances of metal-poor stars have been used to study the detailed physics of thermonuclear explosions (e.g., Reyes et al. 2020). Because cobalt and zinc nucleosynthesis in core-collapse supernovae is correlated with explosion energy, the low abundances of $[\text{Co}/\text{Fe}]$ and $[\text{Zn}/\text{Fe}]$ in our three IRMP stars suggest that powerful core-collapse supernovae did not contribute much to the iron-peak abundances of our three IRMP stars.

4.4. Neutron-capture Elements

Elements with atomic numbers $Z \gtrsim 30$ like strontium, yttrium, barium, and europium are often referred to as neutron-capture elements because they are mostly synthesized through the capture of neutrons by existing nuclei. The neutron-capture timescale can be either “slow” or “rapid” relative to β decay timescales. The relative contributions of these s - and r -processes to the nucleosynthesis of each element are different and are functions of metallicity. Some elements like strontium, yttrium, and barium are more commonly used as tracers of the s -process. On the other hand, europium is used as a tracer of r -process nucleosynthesis (e.g., Cescutti et al. 2006;

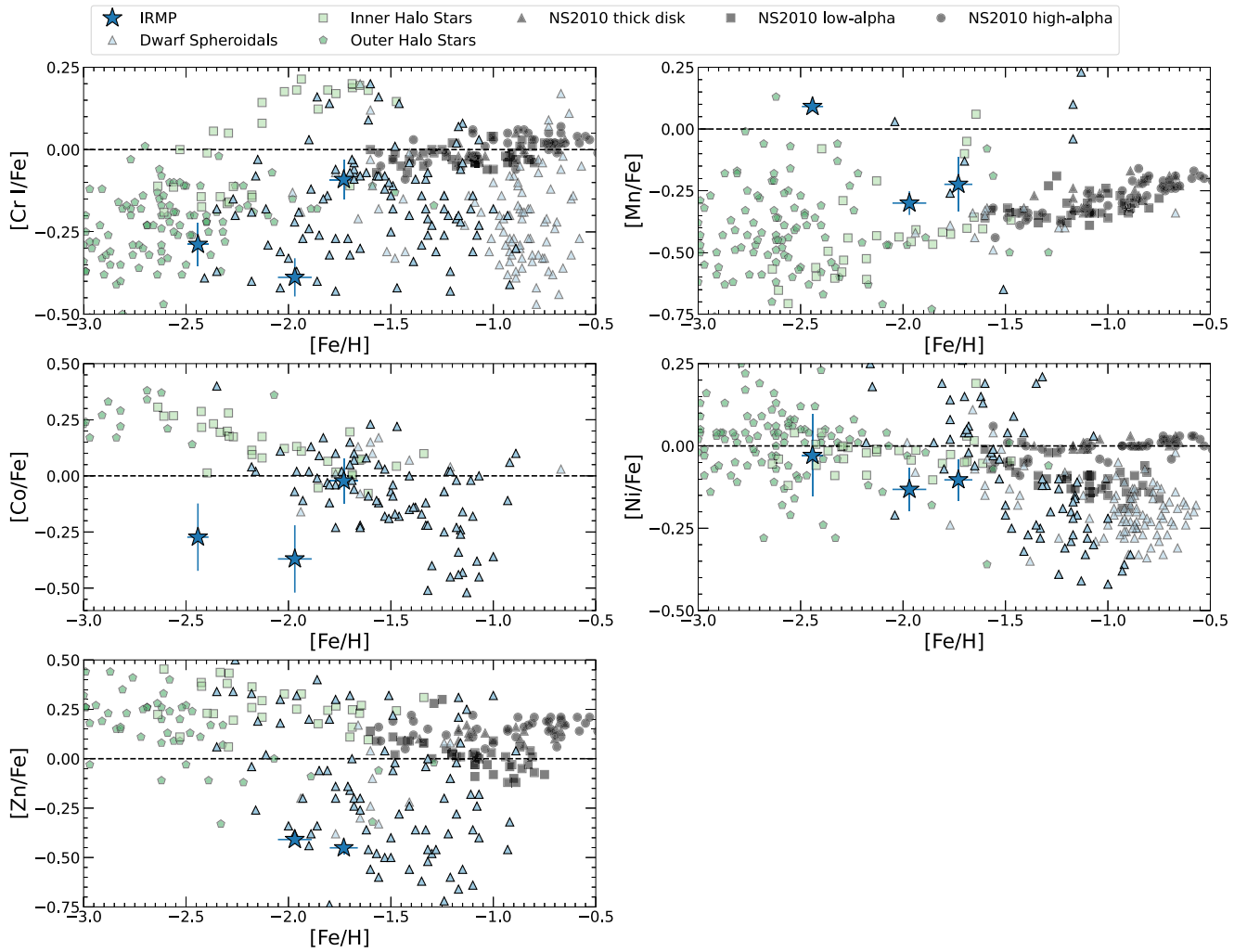


Figure 4. Abundances of the iron-peak elements chromium, manganese, cobalt, nickel, and zinc. We plot as dark-blue stars the three IRMP stars in our sample. We plot as black-bordered light-green squares the inner-halo metal-poor stars from Reggiani et al. (2017) and H. R. Reggiani et al. (2023, in preparation); as dark-gray triangles, squares, and circles thick-disk, low- α , and high- α stars from Nissen & Schuster (2010), respectively; as black-bordered light-blue triangles stars from the dSph galaxies Carina, Fornax, Sagittarius, and Sculptor (Shetrone et al. 2003; Geisler et al. 2005; Monaco et al. 2005; Letarte et al. 2010; Hill et al. 2019; Skúladóttir et al. 2019); and as dark-green pentagons outer-halo metal-poor stars from Cayrel et al. (2004) and Jacobson et al. (2015). By construction, our three IRMP stars have low [Co/Fe]. The high [Mn/Fe] abundances we infer support the idea that the iron-peak elements in IRMP stars were mostly synthesized in thermonuclear supernovae.

Jacobson & Friel 2013; Ji et al. 2016). Strontium, yttrium, and europium abundance inferences based on the lines we use are not strongly affected by departures from the assumptions of LTE. We correct barium abundances for departures from the assumptions of LTE using data from Amarsi et al. (2020).

We report in Table 4 the strontium, yttrium, barium, and europium abundances we infer for the three IRMP stars in our sample and plot them in Figure 5 along with several comparison samples. In accord with our comparison samples, we plot in Figure 5 Sr II abundances that are insensitive to departures from the assumptions of LTE (e.g., Hansen et al. 2013). At $[\text{Fe}/\text{H}] \gtrsim -2$, the $[\text{Sr}/\text{Fe}]$ abundances we observe are very low. Likewise, the $[\text{Ba}/\text{Fe}]$ and $[\text{Eu}/\text{Fe}]$ abundances we infer for BD +80°0245 and HE 0533–5340 are very low. Since essentially no neutron-capture elements are synthesized in thermonuclear explosions, the low neutron-capture abundances relative to iron we see in our three IRMP stars support our assertion that IRMP stars formed in environments where the contribution of thermonuclear events to iron-peak nucleosynthesis was above average. On the other hand, the star SMSS

J034249.53–284216.0 has supersolar $[\text{Eu}/\text{Ba}]$, mildly enhanced $[\text{Eu}/\text{Fe}]$, and highly enhanced $[\text{Eu}/\text{Mg}]$. These three facts could possibly result from a prolific r -process nucleosynthesis that occurred before the thermonuclear event that produced most of its iron content.

5. Discussion

We homogeneously analyzed the orbital properties, photospheric stellar parameters, and elemental abundances of three giant stars BD +80°245, HE 0533–5340, and SMSS J034249.53–284216.0 with $[\text{Fe}/\text{H}] < -1$ plus literature abundances $[\text{Na}, \text{Mg}, \text{Co}/\text{Fe}] < 0$ placing them in a sparsely populated region of elemental abundance space consistent with predictions for thermonuclear nucleosynthesis. We found that these three stars have low-eccentricity orbits with apocenters inside 15 kpc typical of inner-halo stars and therefore no orbital indication that they formed in dwarf galaxies like the stars similarly studied in Reggiani et al. (2022b).

Our state-of-the-art homogeneous abundance analyses confirmed that these three stars have $[\text{Na}, \text{Mg}, \text{Al}, \text{Co}, \text{Zn}, \text{Sr}, \text{Ba}/$

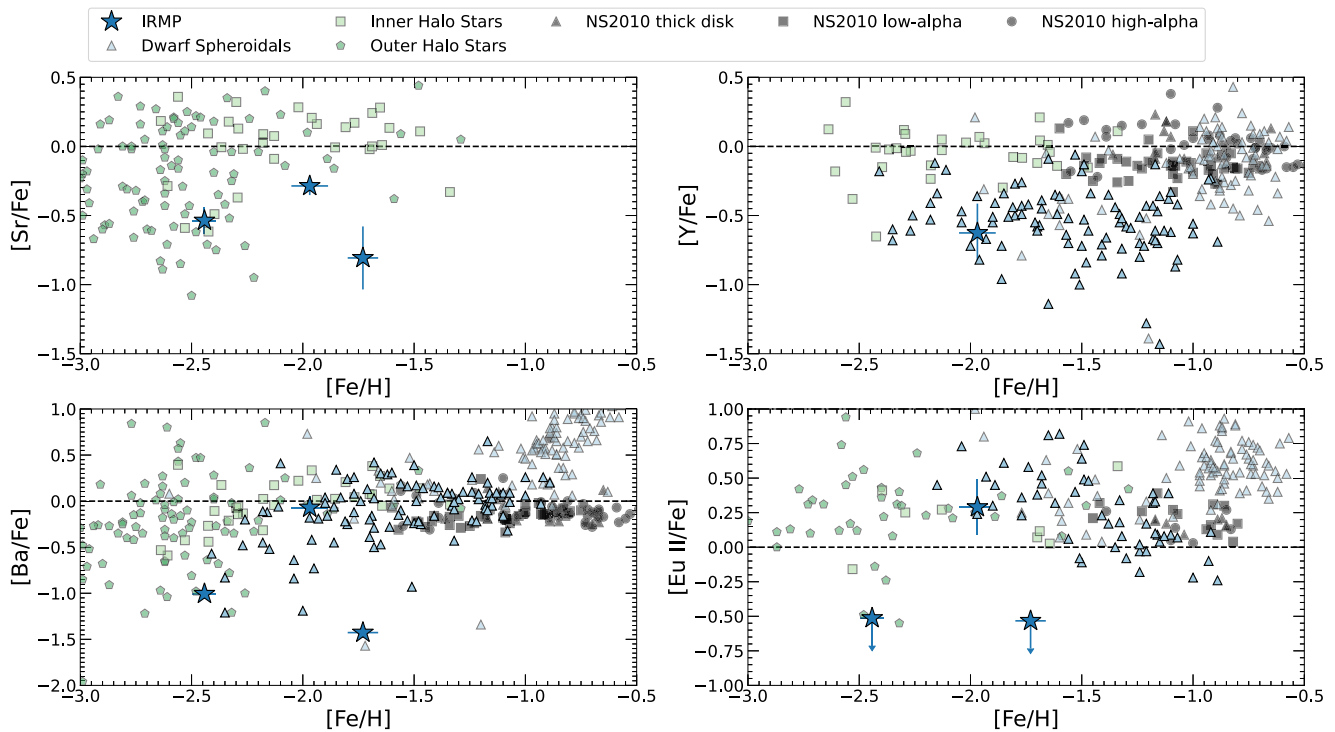


Figure 5. Abundances of the neutron-capture elements strontium, yttrium, barium, and europium. We plot as black-bordered light-green squares inner-halo metal-poor stars from Reggiani et al. (2017) and H. R. Reggiani et al. (2023, in preparation); as dark-gray triangles, squares, and circles thick-disk, low- α , and high- α stars from Nissen & Schuster (2010), respectively; as black-bordered light-blue triangles stars from the dSph galaxies Carina, Fornax, Sagittarius, and Sculptor (Shetrone et al. 2003; Geisler et al. 2005; Monaco et al. 2005; Letarte et al. 2010; Hill et al. 2019; Skúladóttir et al. 2019); and as dark-green pentagons outer-halo metal-poor stars from Cayrel et al. (2004) and Jacobson et al. (2015). As essentially no neutron-capture elements are synthesized in thermonuclear explosions, the low neutron-capture abundances relative to iron we infer support the idea that the iron-peak elements in IRMP stars were mostly synthesized in thermonuclear events without the additional neutron-capture elements expected under more typical chemical evolution scenarios.

$[\text{Fe}] < 0$ as expected if they formed in environments dominated by thermonuclear nucleosynthesis. When compared to samples of inner-halo, outer-halo, and classical dSph galaxy stars, BD +80°245, HE 0533–5340, and SMSS J034249.53–284216.0 have low $[\text{Mg}/\text{Fe}]$, $[\text{Ca}/\text{Fe}]$, $[\text{Ti}/\text{Fe}]$, $[\text{Na}/\text{Fe}]$, $[\text{Sc}/\text{Fe}]$, $[\text{Co}/\text{Fe}]$, $[\text{Zn}/\text{Fe}]$, $[\text{Sr}/\text{Fe}]$, and $[\text{Ba}/\text{Fe}]$ abundances. They have high $[\text{Mn}/\text{Fe}]$ abundances. BD +80°245 and HE 0533–5340 have very low upper limits $[\text{Eu}/\text{Fe}] \lesssim -0.5$, while SMSS J034249.53–284216.0 has a more ordinary $[\text{Eu}/\text{Fe}] = 0.29$. Because most manganese and essentially no neutron-capture elements are synthesized in thermonuclear explosions, the relatively high $[\text{Mn}/\text{Fe}]$ abundances combined with the relatively low $[\text{Sr}/\text{Fe}]$ and $[\text{Ba}/\text{Fe}]$ abundances in these three stars support the idea that they formed in environments dominated by thermonuclear nucleosynthesis. Our results are consistent with previous conclusions based on similar stars (e.g., Ivans et al. 2003; Aoki et al. 2014; Jeong et al. 2023). As we will show, though, we are able to constrain specific thermonuclear explosion mechanisms. We argue that these three stars are part of a class of metal-poor stars we refer to as IRMP stars.

The abundance properties shared between these three IRMP stars can be used to explore the population of thermonuclear explosions. The low $[\text{Ca}/\text{Fe}]$ and $[\text{Ti}/\text{Fe}]$ abundances of these three IRMP stars disfavor thermonuclear explosions produced by direct white dwarf collisions or spot- or belt-like double detonations with either especially thin or especially thick helium envelopes. Similarly, the low $[\text{Sc}/\text{Fe}]$ abundance of these three IRMP stars disfavors double detonations in thick helium envelopes.

In an attempt to derive more specific constraints on the thermonuclear explosions responsible for the abundance patterns we observe in these three IRMP stars, we fit the grids of theoretical thermonuclear supernova yields from Seitzzahl et al. (2013, 2016), Fink et al. (2014), Ohlmann et al. (2014), Papish & Perets (2016), Seitzzahl et al. (2016), Leung & Nomoto (2018), Nomoto & Leung (2018), Bravo et al. (2019), Leung & Nomoto (2020a, 2020b), Gronow et al. (2021a, 2021b), Boos et al. (2021), and Neopane et al. (2022) to select the individual models that predict abundances closest to those we observed in our sample. Because both core-collapse supernovae with delay times of a few megayears and thermonuclear supernovae with delay times of a few tens of megayears contributed to the metal contents of our three IRMP stars, we use a χ^2 -like statistic to select the individual models that best predict our observed abundances. Since we argue that a thermonuclear explosion produced the iron-peak elements we observe in our three IRMP stars, we use the usual definition of χ^2 to assess the ability of the theoretical models listed above to reproduce our observations. On the other hand, one or more core-collapse supernovae combined with a thermonuclear explosion to produce the α -element and light odd- Z element abundance we observed. As a result, we only penalize thermonuclear explosions that produce α -element and light odd- Z element abundances beyond the level we observed. We exclude from our χ^2 -like statistic individual elemental abundances for which a theoretical model predicts α -element and light odd- Z element abundances below the level we observed.

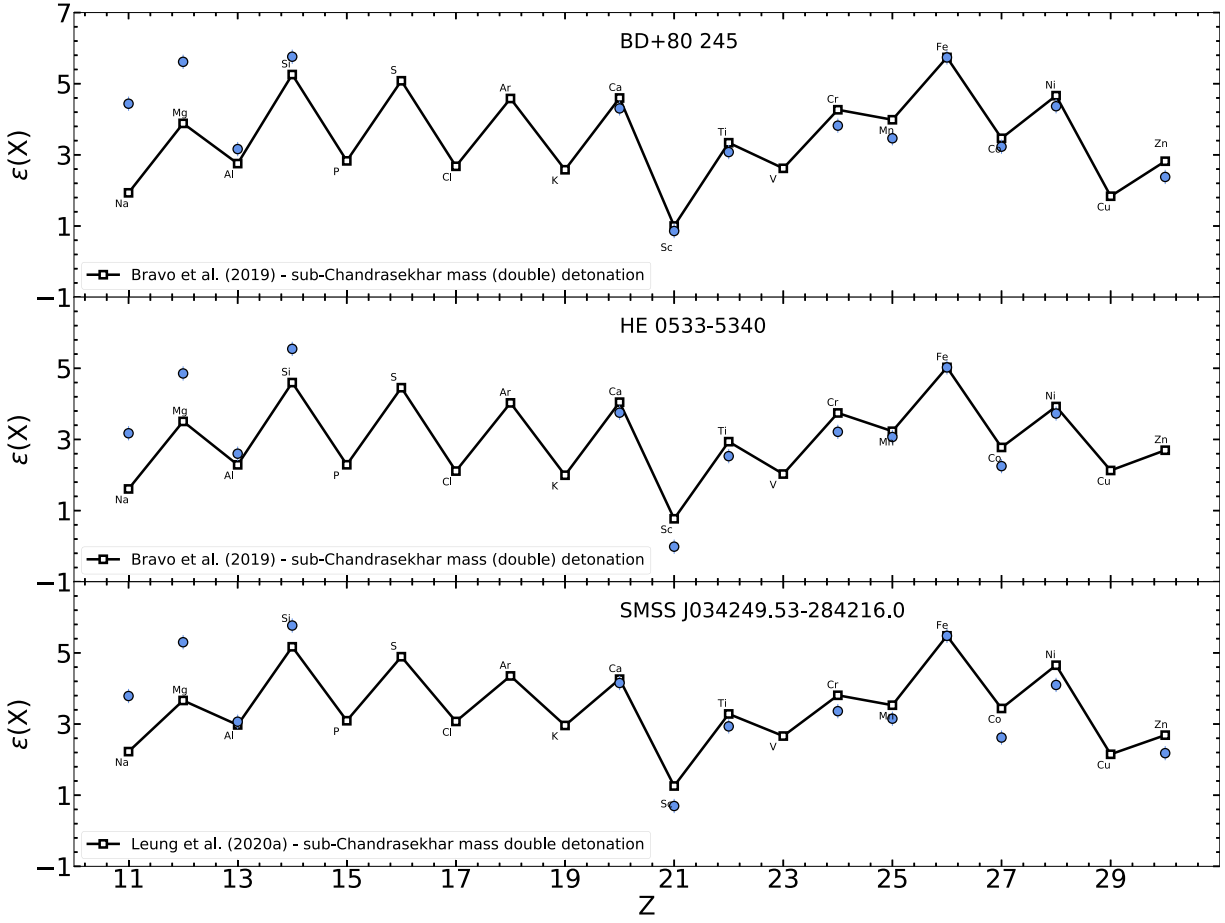


Figure 6. Observed elemental abundances and predicted thermonuclear event yields from models that best fit the observed data. We plot as blue circles our observed elemental abundances and as black-bordered white squares connected by solid black lines the theoretical yields predicted by the model that best reproduces our observations. The best model in each panel is depicted as black open squares, and the inferred stellar abundances are shown as blue circles. The abundances of BD +80°245 and HE 0533–5340 are best fit by Bravo et al. (2019) models for the detonation of sub-Chandrasekhar-mass CO white dwarfs with $M_{\text{WD}} = 1.1 M_{\odot}$, a standard C/O ratio, and metallicities of $Z = 9 \times 10^{-3}$ and $Z = 2.25 \times 10^{-3}$, respectively. The abundances of SMSS J034249.53–284216.0 are best fit by the Leung & Nomoto (2020a) sub-Chandrasekhar-mass double-detonation model 110-050-2-S50.

To carry out the procedure described above, we first normalize the iron yield of each model to the $[\text{Fe}/\text{H}]$ value we infer for each star. We then identify the model that minimizes the modified χ^2 statistic we define as

$$\chi^2 = \sum_i f([\text{X}_i/\text{Fe}]_o, [\text{X}_i/\text{Fe}]_p) \frac{([\text{X}_i/\text{Fe}]_o - [\text{X}_i/\text{Fe}]_p)^2}{\sigma_{[\text{X}_i/\text{Fe}]_o}} + \sum_j \frac{([\text{X}_j/\text{Fe}]_o - [\text{X}_j/\text{Fe}]_p)^2}{\sigma_{[\text{X}_j/\text{Fe}]_o}}, \quad (1)$$

where $[\text{X}/\text{Fe}]_o$ represents our observed abundances, $[\text{X}/\text{Fe}]_p$ represents predicted abundances, and $\sigma_{[\text{X}/\text{Fe}]_o}$ represents the uncertainties in our observed abundances. The first summation is taken over the α - and light odd- Z elements sodium, magnesium, aluminum, silicon, calcium, scandium, and titanium. The second summation is taken over the iron-peak elements chromium, manganese, cobalt, nickel, and zinc. We define the function $f([\text{X}/\text{Fe}]_o, [\text{X}/\text{Fe}]_p)$ as

$$f([\text{X}/\text{Fe}]_o, [\text{X}/\text{Fe}]_p) \equiv \begin{cases} 1 & \text{if } [\text{X}/\text{Fe}]_o \leq [\text{X}/\text{Fe}]_p \\ 0 & \text{if } [\text{X}/\text{Fe}]_o > [\text{X}/\text{Fe}]_p. \end{cases} \quad (2)$$

We plot the abundances of BD +80°245, HE 0533–5340, and SMSS J034249.53–284216.0 along with the models that

best fit those abundances in Figure 6. We find that BD +80°245 and HE 0533–5340 are best fit by Bravo et al. (2019) models for the detonation of sub-Chandrasekhar-mass CO white dwarfs with $M_{\text{WD}} = 1.1 M_{\odot}$, a standard C/O ratio, and metallicities of $Z = 9 \times 10^{-3}$ and $Z = 2.25 \times 10^{-3}$, respectively. In the one-dimensional Bravo et al. (2019) models the detonation is arbitrarily sparked at the center of the white dwarf. This could be a spontaneous pure detonation, a double detonation triggered by the detonation of a thin surface helium shell, or a detonation resulting from the merger of a double-degenerate system. The abundances of SMSS J034249.53–284216.0 are best fit by the Leung & Nomoto (2020a) sub-Chandrasekhar-mass double-detonation model 110-050-2-S50.

If our interpretation of IRMP stars is correct, then the occurrence of IRMP stars should depend on galactic environment. It is well established that at constant $[\text{Fe}/\text{H}] \gtrsim -2.5$ surviving dSph galaxies have lower $[\alpha/\text{Fe}]$ abundances than Milky Way halo stars. The usual interpretation of this observation is that the surviving dSph galaxies had extended star formation histories, implying that thermonuclear nucleosynthesis was relatively more important for the chemical evolution of dSph galaxies than for the Milky Way’s halo (e.g., Tolstoy et al. 2009; Kirby et al. 2011a, 2011b; Brown et al. 2012; Vargas et al. 2013; Brown et al. 2014; Weisz et al. 2014).

Reggiani et al. (2021) showed that at $[\text{Fe}/\text{H}] \gtrsim -2$ the same is true in the Magellanic Clouds. On the other hand, the Milky Way’s globular clusters consistently have $[\alpha/\text{Fe}] \approx 0.4$, characteristically of core-collapse supernova nucleosynthesis. We assert that the occurrence of IRMP stars should be correlated with the relative importance of thermonuclear nucleosynthesis to the chemical evolution of a particular environment. We predict that IRMP stars should be more common in surviving dSph galaxies and the Magellanic Clouds than in the Milky Way. We further predict that IRMP stars should be rare in globular clusters.

6. Conclusions

We collected published nucleosynthesis predictions for thermonuclear explosions that could be responsible for the astrophysical transients observationally classified as Type Ia supernovae. We find that thermonuclear explosion models that yield $M_{\text{Fe}} \geq 0.1 M_{\odot}$ always produce $[\text{C}, \text{N}, \text{O}, \text{F}, \text{Ne}, \text{Na}, \text{Mg}, \text{Al}, \text{Cl}, \text{K}, \text{Co}, \text{Cu}, \text{Zn}/\text{Fe}] < 0$, an abundance space rarely populated by metal-poor stars with $[\text{Fe}/\text{H}] < -1$. Focusing on the subset of these elements readily observable in the photospheres of metal-poor giants stars $[\text{Na}, \text{Mg}, \text{Co}/\text{Fe}] < 0$, we selected from the Stellar Abundances for Galactic Archaeology database three metal-poor giants in this region of abundance space: BD +80°245, HE 0533–5340, and SMSS J034249.53–284216.0. We characterized the Galactic orbits of these three stars and found no reason to believe that they formed in now-disrupted dSph galaxies. We executed a state-of-the-art, homogeneous abundance analysis for these three stars and confirmed that they have $[\text{Na}, \text{Mg}, \text{Al}, \text{Co}, \text{Zn}, \text{Sr}, \text{Ba}/\text{Fe}] < 0$ as expected if they formed in environments dominated by thermonuclear nucleosynthesis. We argue that these three metal-poor stars BD +80°245, HE 0533–5340, and SMSS J034249.53–284216.0 should be considered the first examples of a new class of metal-poor stars that we refer to as IRMP stars that formed in environments dominated by thermonuclear nucleosynthesis. The elemental abundances of these three stars disfavor thermonuclear explosions produced by direct white dwarf collisions or double detonations in either very thin or very thick helium shells. The elemental abundances of BD +80°245, HE 0533–5340, and SMSS J034249.53–284216.0 are best explained by the (double) detonation of sub-Chandrasekhar-mass CO white dwarfs. If our interpretation of IRMP stars is correct, then they should be very rare in globular clusters and more common in the Magellanic Clouds and dSph galaxies than in the Milky Way halo.

Acknowledgments

We thank Ian Roederer, Ian Thompson, and Heather Jacobson for providing us with their spectra of BD +80°245, HE 0533–5340, and SMSS J034249.53–284216.0. We thank Abigail Polin and Yossef Zenati for numerous helpful discussions about the physics of thermonuclear explosions and the observational properties of Type Ia supernovae. H.R. acknowledges support from a Carnegie Fellowship. Parts of this research were supported by the Australian Research Council Centre of Excellence for All Sky Astrophysics in 3 Dimensions (ASTRO 3D), through project No. CE170100013. The national facility capability for SkyMapper has been funded through ARC LIEF grant LE130100104 from the Australian

Research Council, awarded to the University of Sydney, the Australian National University, Swinburne University of Technology, the University of Queensland, the University of Western Australia, the University of Melbourne, Curtin University of Technology, Monash University, and the Australian Astronomical Observatory. SkyMapper is owned and operated by the Australian National University’s Research School of Astronomy and Astrophysics. The survey data were processed and provided by the SkyMapper Team at ANU. The SkyMapper node of the All-Sky Virtual Observatory (ASVO) is hosted at the National Computational Infrastructure (NCI). Development and support of the SkyMapper node of the ASVO have been funded in part by Astronomy Australia Limited (AAL) and the Australian Government through the Commonwealth’s Education Investment Fund (EIF) and National Collaborative Research Infrastructure Strategy (NCRIS), particularly the National eResearch Collaboration Tools and Resources (NeCTAR) and the Australian National Data Service Projects (ANDS). This work has made use of data from the European Space Agency (ESA) mission Gaia (<https://www.cosmos.esa.int/gaia>), processed by the Gaia Data Processing and Analysis Consortium (DPAC, <https://www.cosmos.esa.int/web/gaia/dpac/consortium>). Funding for the DPAC has been provided by national institutions, in particular the institutions participating in the Gaia Multilateral Agreement. This publication makes use of data products from the Two Micron All Sky Survey, which is a joint project of the University of Massachusetts and the Infrared Processing and Analysis Center/California Institute of Technology, funded by the National Aeronautics and Space Administration and the National Science Foundation. This publication makes use of data products from the Wide-field Infrared Survey Explorer, which is a joint project of the University of California, Los Angeles, and the Jet Propulsion Laboratory/California Institute of Technology, funded by the National Aeronautics and Space Administration. This research has made use of the NASA/IPAC Infrared Science Archive, which is funded by the National Aeronautics and Space Administration and operated by the California Institute of Technology. This research has made use of the SIMBAD database, operated at CDS, Strasbourg, France (Wenger et al. 2000). This research has made use of the VizieR catalog access tool, CDS, Strasbourg, France (DOI:10.26093/cds/vizieR). The original description of the VizieR service was published in 2000, A&AS 143, 23 (Ochsenbein et al. 2000). This research has made use of the Keck Observatory Archive (KOA), which is operated by the W. M. Keck Observatory and the NASA Exoplanet Science Institute (NExScI), under contract with the National Aeronautics and Space Administration. This research has made use of NASA’s Astrophysics Data System Bibliographic Services.

Facilities: ADS, CDS, CTIO:2MASS, FLWO:2MASS, Gaia, GALEX, KOA, IRSA, Magellan:Clay, NEOWISE, SkyMapper, Smith, WISE.

Software: `astropy` (Astropy Collaboration et al. 2013, 2018), `colte` (Casagrande et al. 2021), `isochrones` (Morton 2015), `MOOG` (Snedden 1973), `MultiNest` (Feroz & Hobson 2008; Feroz et al. 2009, 2019), `numpy` (Harris et al. 2020), `pandas` (McKinney 2010; Reback et al. 2020), `PyMultiNest` (Buchner et al. 2014), `q2` (Ramírez et al. 2014), `R` (R Core Team 2022), `scipy` (Virtanen et al. 2020).

ORCID iDs

Henrique Reggiani  <https://orcid.org/0000-0001-6533-6179>Kevin C. Schlaufman  <https://orcid.org/0000-0001-5761-6779>Andrew R. Casey  <https://orcid.org/0000-0003-0174-0564>

References

- Amarsi, A. M., & Asplund, M. 2017, *MNRAS*, **464**, 264
- Amarsi, A. M., Lind, K., Asplund, M., Barklem, P. S., & Collet, R. 2016, *MNRAS*, **463**, 1518
- Amarsi, A. M., Lind, K., Osorio, Y., et al. 2020, *A&A*, **642**, A62
- Aoki, W., Tominaga, N., Beers, T. C., Honda, S., & Lee, Y. S. 2014, *Sci*, **345**, 912
- Arenou, F., Luri, X., Babusiaux, C., et al. 2018, *A&A*, **616**, A17
- Arnett, W. D. 1969, *ApSS*, **5**, 180
- Arnett, W. D., Truran, J. W., & Woosley, S. E. 1971, *ApJ*, **165**, 87
- Asplund, M., Amarsi, A. M., & Grevesse, N. 2021, *A&A*, **653**, A141
- Astropy Collaboration, Price-Whelan, A. M., Sipőcz, B. M., et al. 2018, *AJ*, **156**, 123
- Astropy Collaboration, Robitaille, T. P., Tollerud, E., et al. 2013, *A&A*, **558**, A33
- Badenes, C., Borkowski, K. J., Hughes, J. P., Hwang, U., & Bravo, E. 2006, *ApJ*, **645**, 1373
- Bergemann, M., & Cescutti, G. 2010, *A&A*, **522**, A9
- Bernstein, R., Shtetman, S. A., & Gunnels, S. M. 2003, *Proc. SPIE*, **4841**, 1694
- Bianchi, L., Shiao, B., & Thilker, D. 2017, *ApJS*, **230**, 24
- Bildsten, L., Shen, K. J., Weinberg, N. N., & Nelemans, G. 2007, *ApJL*, **662**, L95
- Bland-Hawthorn, J., & Gerhard, O. 2016, *ARA&A*, **54**, 529
- Boos, S. J., Townsley, D. M., Shen, K. J., Caldwell, S., & Miles, B. J. 2021, *ApJ*, **919**, 126
- Bovy, J. 2015, *ApJS*, **216**, 29
- Branch, D., Doggett, J. B., Nomoto, K., & Thielemann, F. K. 1985, *ApJ*, **294**, 619
- Branch, D., Lacy, C. H., McCall, M. L., et al. 1983, *ApJ*, **270**, 123
- Bravo, E., Badenes, C., & Martínez-Rodríguez, H. 2019, *MNRAS*, **482**, 4346
- Bravo, E., & García-Senz, D. 2008, *A&A*, **478**, 843
- Bravo, E., & García-Senz, D. 2009, *ApJ*, **695**, 1244
- Bravo, E., García-Senz, D., Cabezón, R. M., & Domínguez, I. 2009, *ApJ*, **695**, 1257
- Brown, T. M., Tumlinson, J., Geha, M., et al. 2012, *ApJL*, **753**, L21
- Brown, T. M., Tumlinson, J., Geha, M., et al. 2014, *ApJ*, **796**, 91
- Buchner, J., Georgakakis, A., Nandra, K., et al. 2014, *A&A*, **564**, A125
- Capitania, L., Lallement, R., Vergely, J. L., Elyajouri, M., & Monreal-Ibero, A. 2017, *A&A*, **606**, A65
- Carney, B. W., Wright, J. S., Sneden, C., et al. 1997, *AJ*, **114**, 363
- Casagrande, L., Lin, J., Rains, A. D., et al. 2021, *MNRAS*, **507**, 2684
- Casey, A. R. 2014, PhD thesis, Australian National University
- Castelli, F., & Kurucz, R. L. 2003, in IAU Symp. 210, Modelling of Stellar Atmospheres, Poster Contributions (San Francisco, CA: ASP), A20
- Cayrel, R., Depagne, E., Spite, M., et al. 2004, *A&A*, **416**, 1117
- Cescutti, G., François, P., Matteucci, F., Cayrel, R., & Spite, M. 2006, *A&A*, **448**, 557
- Choi, J., Dotter, A., Conroy, C., et al. 2016, *ApJ*, **823**, 102
- Clayton, D. 2003, *Handbook of Isotopes in the Cosmos* (Cambridge: Cambridge Univ. Press)
- Cohen, J. G., Christlieb, N., Thompson, I., et al. 2013, *ApJ*, **778**, 56
- Colgate, S. A., & McKee, C. 1969, *ApJ*, **157**, 623
- de los Reyes, M. A. C., Kirby, E. N., Seitzzahl, I. R., & Shen, K. J. 2020, *ApJ*, **891**, 85
- Dotter, A. 2016, *ApJS*, **222**, 8
- Evans, D. W., Riello, M., De Angeli, F., et al. 2018, *A&A*, **616**, A4
- Fabrichius, C., Luri, X., Arenou, F., et al. 2021, *A&A*, **649**, A5
- Feroz, F., & Hobson, M. P. 2008, *MNRAS*, **384**, 449
- Feroz, F., Hobson, M. P., & Bridges, M. 2009, *MNRAS*, **398**, 1601
- Feroz, F., Hobson, M. P., Cameron, E., & Pettitt, A. N. 2019, *OJAp*, **2**, 10
- Fink, M., Hillebrandt, W., & Röpke, F. K. 2007, *A&A*, **476**, 1133
- Fink, M., Kromer, M., Seitzzahl, I. R., et al. 2014, *MNRAS*, **438**, 1762
- Fink, M., Röpke, F. K., Hillebrandt, W., et al. 2010, *A&A*, **514**, A53
- Frebel, A., Casey, A. R., Jacobson, H. R., & Yu, Q. 2013, *ApJ*, **769**, 57
- Fulbright, J. P. 2000, *AJ*, **120**, 1841
- Gaia Collaboration, Brown, A. G. A., Vallenari, A., et al. 2018, *A&A*, **616**, A1
- Gaia Collaboration, Prusti, T., de Bruijne, J. H. J., et al. 2016, *A&A*, **595**, A1
- Gamezo, V. N., Khokhlov, A. M., & Oran, E. S. 2004, *PhRvL*, **92**, 211102
- Gamezo, V. N., Khokhlov, A. M., & Oran, E. S. 2005, *ApJ*, **623**, 337
- Gamezo, V. N., Khokhlov, A. M., Oran, E. S., Chtchelkanova, A. Y., & Rosenberg, R. O. 2003, *Sci*, **299**, 77
- Geisler, D., Smith, V. V., Wallerstein, G., Gonzalez, G., & Charbonnel, C. 2005, *AJ*, **129**, 1428
- Gravity Collaboration, Abuter, R., Amorim, A., et al. 2018, *A&A*, **615**, L15
- Green, G. M., Schlafly, E., Zucker, C., Speagle, J. S., & Finkbeiner, D. 2019, *ApJ*, **887**, 93
- Grimmett, J. J., Karakas, A. I., Heger, A., Müller, B., & West, C. 2020, *MNRAS*, **496**, 4987
- Gronow, S., Collins, C. E., Sim, S. A., & Röpke, F. K. 2021a, *A&A*, **649**, A155
- Gronow, S., Côté, B., Lach, F., et al. 2021b, *A&A*, **656**, A94
- Guillochon, J., Dan, M., Ramirez-Ruiz, E., & Rosswog, S. 2010, *ApJL*, **709**, L64
- Hambly, N. C., Cropper, M., Boudreault, S., et al. 2018, *A&A*, **616**, A15
- Hansen, C. J., Bergemann, M., Cescutti, G., et al. 2013, *A&A*, **551**, A57
- Harris, C. R., Millman, K. J., van der Walt, S. J., et al. 2020, *Natur*, **585**, 357
- Hill, V., Skúladóttir, Á., Tolstoy, E., et al. 2019, *A&A*, **626**, A15
- Hillebrandt, W., Kromer, M., Röpke, F. K., & Ruiter, A. J. 2013, *FrPhy*, **8**, 116
- Hoeflich, P., & Khokhlov, A. 1996, *ApJ*, **457**, 500
- Hoyle, F., & Fowler, W. A. 1960, *ApJ*, **132**, 565
- Ivans, I. I., Sneden, C., James, C. R., et al. 2003, *ApJ*, **592**, 906
- Jacobson, H. R., & Friel, E. D. 2013, *AJ*, **145**, 107
- Jacobson, H. R., Keller, S., Frebel, A., et al. 2015, *ApJ*, **807**, 171
- Jeong, M., Lee, Y. S., Beers, T. C., et al. 2023, *ApJ*, **948**, 38
- Jermyn, A. S., Bauer, E. B., Schwab, J., et al. 2023, *ApJS*, **265**, 15
- Ji, A. P., Frebel, A., Chiti, A., & Simon, J. D. 2016, *Natur*, **531**, 610
- Ji, A. P., Li, T. S., Simon, J. D., et al. 2020, *ApJ*, **889**, 27
- Jordan, G. C. I., Fisher, R. T., Townsley, D. M., et al. 2008, *ApJ*, **681**, 1448
- Jordan, G. C. I., Graziani, C., Fisher, R. T., et al. 2012, *ApJ*, **759**, 53
- Jurić, M., Ivezić, Ž., Brooks, A., et al. 2008, *ApJ*, **673**, 864
- Kelson, D. D. 2003, *PASP*, **115**, 688
- Kelson, D. D., Illingworth, G. D., van Dokkum, P. G., & Franx, M. 2000, *ApJ*, **531**, 159
- Kelson, D. D., Williams, R. J., Dressler, A., et al. 2014, *ApJ*, **783**, 110
- Khokhlov, A. M. 1991, *A&A*, **245**, 114
- Kirby, E. N., Cohen, J. G., Smith, G. H., et al. 2011a, *ApJ*, **727**, 79
- Kirby, E. N., Lanfranchi, G. A., Simon, J. D., Cohen, J. G., & Guhathakurta, P. 2011b, *ApJ*, **727**, 78
- Kirshner, R. P., Jeffery, D. J., Leibundgut, B., et al. 1993, *ApJ*, **415**, 589
- Klose, J. Z., Fuhr, J. R., & Wiese, W. L. 2002, *JPCRD*, **31**, 217
- Kobayashi, C., Karakas, A. I., & Lugaro, M. 2020a, *ApJ*, **900**, 179
- Kobayashi, C., Leung, S.-C., & Nomoto, K. 2020b, *ApJ*, **895**, 138
- Korn, A. J., Shi, J., & Gehren, T. 2003, *A&A*, **407**, 691
- Kromer, M., Ohlmann, S. T., Pakmor, R., et al. 2015, *MNRAS*, **450**, 3045
- Kushnir, D., Katz, B., Dong, S., Livne, E., & Fernández, R. 2013, *ApJL*, **778**, L37
- Lallement, R., Capitania, L., Ruiz-Dern, L., et al. 2018, *A&A*, **616**, A132
- Lallement, R., Vergely, J. L., Valette, B., et al. 2014, *A&A*, **561**, A91
- Letarte, B., Hill, V., Tolstoy, E., et al. 2010, *A&A*, **523**, A17
- Leung, S.-C., & Nomoto, K. 2018, *ApJ*, **861**, 143
- Leung, S.-C., & Nomoto, K. 2020a, *ApJ*, **888**, 80
- Leung, S.-C., & Nomoto, K. 2020b, *ApJ*, **900**, 54
- Lind, K., Asplund, M., Barklem, P. S., & Belyaev, A. K. 2011, *A&A*, **528**, A103
- Lindgren, L., Bastian, U., Biermann, M., et al. 2021a, *A&A*, **649**, A4
- Lindgren, L., Klioner, S. A., Hernández, J., et al. 2021b, *A&A*, **649**, A2
- Livne, E. 1990, *ApJL*, **354**, L53
- Livne, E., & Arnett, D. 1995, *ApJ*, **452**, 62
- Mainzer, A., Grav, T., Bauer, J., et al. 2011, *ApJ*, **743**, 156
- Maoz, D., Mannucci, F., & Nelemans, G. 2014, *ARA&A*, **52**, 107
- Mazzali, P. A., Lucy, L. B., Danziger, I. J., et al. 1993, *A&A*, **269**, 423
- McKinney, W. 2010, in Proc. of the 9th Python in Science Conf., ed. S. van der Walt & J. Millman (Austin, TX: SciPy), 56
- McWilliam, A. 1998, *AJ*, **115**, 1640
- Minkowski, R. 1964, *ARA&A*, **2**, 247
- Mishenina, T., Pignatari, M., Côté, B., et al. 2017, *MNRAS*, **469**, 4378
- Miyamoto, M., & Nagai, R. 1975, *PASJ*, **27**, 533
- Monaco, L., Bellazzini, M., Bonifacio, P., et al. 2005, *A&A*, **441**, 141
- Morton, T. D. 2015, Isochrones: Stellar model grid package, Astrophysics Source Code Library, ascl:1503.01000
- Mucciarelli, A., & Bonifacio, P. 2020, *A&A*, **640**, A87

- Navarro, J. F., Frenk, C. S., & White, S. D. M. 1996, *ApJ*, 462, 563
- Neopane, S., Bhargava, K., Fisher, R., et al. 2022, *ApJ*, 925, 92
- Nissen, P. E., & Schuster, W. J. 2010, *A&A*, 511, L10
- Nomoto, K. 1982a, *ApJ*, 253, 798
- Nomoto, K. 1982b, *ApJ*, 257, 780
- Nomoto, K., & Leung, S.-C. 2018, *SSRv*, 214, 67
- Nomoto, K., Sugimoto, D., & Neo, S. 1976, *Ap&SS*, 39, L37
- Nomoto, K., Thielemann, F. K., & Yokoi, K. 1984, *ApJ*, 286, 644
- Nugent, P., Baron, E., Branch, D., Fisher, A., & Hauschildt, P. H. 1997, *ApJ*, 485, 812
- Ochsenbein, F., Bauer, P., & Marcout, J. 2000, *A&AS*, 143, 23
- Ohlmann, S. T., Kromer, M., Fink, M., et al. 2014, *A&A*, 572, A57
- Onken, C. A., Wolf, C., Bessell, M. S., et al. 2019, *PASA*, 36, e033
- Osorio, Y., Barklem, P. S., Lind, K., et al. 2015, *A&A*, 579, A53
- Pakmor, R., Hachinger, S., Röpke, F. K., & Hillebrandt, W. 2011, *A&A*, 528, A117
- Pakmor, R., Kromer, M., Röpke, F. K., et al. 2010, *Natur*, 463, 61
- Pakmor, R., Kromer, M., Taubenberger, S., et al. 2012, *ApJL*, 747, L10
- Pakmor, R., Kromer, M., Taubenberger, S., & Springel, V. 2013, *ApJL*, 770, L8
- Pankey, T. J. 1962, PhD thesis (Howard University)
- Papish, O., & Perets, H. B. 2016, *ApJ*, 822, 19
- Paxton, B., Bildsten, L., Dotter, A., et al. 2011, *ApJS*, 192, 3
- Paxton, B., Cantiello, M., Arras, P., et al. 2013, *ApJS*, 208, 4
- Paxton, B., Marchant, P., Schwab, J., et al. 2015, *ApJS*, 220, 15
- Paxton, B., Schwab, J., Bauer, E. B., et al. 2018, *ApJS*, 234, 34
- Paxton, B., Smolec, R., Schwab, J., et al. 2019, *ApJS*, 243, 10
- Perlmutter, S., Aldering, G., Goldhaber, G., et al. 1999, *ApJ*, 517, 565
- Phillips, M. M. 1993, *ApJL*, 413, L105
- Piro, A. L. 2008, *ApJ*, 679, 616
- Piro, A. L., & Bildsten, L. 2008, *ApJ*, 673, 1009
- Piro, A. L., & Chang, P. 2008, *ApJ*, 678, 1158
- Placco, V. M., Sneden, C., Roederer, I. U., et al. 2021, *RNAAS*, 5, 92
- Plewa, T., Calder, A. C., & Lamb, D. Q. 2004, *ApJL*, 612, L37
- Prantzos, N., Abia, C., Limongi, M., Chieffi, A., & Cristallo, S. 2018, *MNRAS*, 476, 3432
- Price-Whelan, A., Sipőcz, B., Lenz, D., et al. 2020, *adrn/gala: v1.3*, Zenodo, doi:10.5281/zenodo.4159870
- Price-Whelan, A. M. 2017, *JOSS*, 2, 388
- R Core Team 2017, *OJS*, 7, 859
- Ramírez, I., Meléndez, J., Bean, J., et al. 2014, *A&A*, 572, A48
- Reback, J., McKinney, W., Jbrockmendel, et al. 2020, *pandas-dev/pandas: Pandas v1.2.0*, Zenodo, doi:10.5281/zenodo.4394318
- Reggiani, H., Ji, A. P., Schlaufman, K. C., et al. 2022a, *AJ*, 163, 252
- Reggiani, H., Meléndez, J., Kobayashi, C., Karakas, A., & Placco, V. 2017, *A&A*, 608, A46
- Reggiani, H., Schlaufman, K. C., Casey, A. R., & Ji, A. P. 2020, *AJ*, 160, 173
- Reggiani, H., Schlaufman, K. C., Casey, A. R., Simon, J. D., & Ji, A. P. 2021, *AJ*, 162, 229
- Reggiani, H., Schlaufman, K. C., Healy, B. F., Lothringer, J. D., & Sing, D. K. 2022b, *AJ*, 163, 159
- Riello, M., De Angeli, F., Evans, D. W., et al. 2018, *A&A*, 616, A3
- Riess, A. G., Filippenko, A. V., Challis, P., et al. 1998, *AJ*, 116, 1009
- Roederer, I. U., Preston, G. W., Thompson, I. B., et al. 2014, *AJ*, 147, 136
- Röpke, F. K., & Niemeyer, J. C. 2007, *A&A*, 464, 683
- Rosswog, S., Kasen, D., Guillochon, J., & Ramirez-Ruiz, E. 2009, *ApJL*, 705, L128
- Schlafly, E. F., & Finkbeiner, D. P. 2011, *ApJ*, 737, 103
- Schlegel, D. J., Finkbeiner, D. P., & Davis, M. 1998, *ApJ*, 500, 525
- Schwab, J., Martínez-Rodríguez, H., Piro, A. L., & Badenes, C. 2017, *ApJ*, 851, 105
- Seitzzahl, I. R., Ciaraldi-Schoolmann, F., & Röpke, F. K. 2011, *MNRAS*, 414, 2709
- Seitzzahl, I. R., Ciaraldi-Schoolmann, F., Röpke, F. K., et al. 2013, *MNRAS*, 429, 1156
- Seitzzahl, I. R., Kromer, M., Ohlmann, S. T., et al. 2016, *A&A*, 592, A57
- Shectman, S. A., & Johns, M. 2003, *Proc. SPIE*, 4837, 910
- Shetrone, M., Venn, K. A., Tolstoy, E., et al. 2003, *AJ*, 125, 684
- Skúladóttir, Á., Hansen, C. J., Salvadori, S., & Choplin, A. 2019, *A&A*, 631, A171
- Skrutskie, M. F., Cutri, R. M., Stiening, R., et al. 2006, *AJ*, 131, 1163
- Snedén, C., Lawler, J. E., Cowan, J. J., Ivans, I. I., & Den Hartog, E. A. 2009, *ApJS*, 182, 80
- Snedén, C., Lawler, J. E., den Hartog, E. A., & Wood, M. E. 2016, *IAUFM*, 29A, 287
- Snedén, C. A. 1973, PhD thesis, the university of texas at austin
- Stephens, A., & Boesgaard, A. M. 2002, *AJ*, 123, 1647
- Suda, T., Hidaka, J., Aoki, W., et al. 2017, *PASJ*, 69, 76
- Suda, T., Katsuta, Y., Yamada, S., et al. 2008, *PASJ*, 60, 1159
- Suda, T., Yamada, S., Katsuta, Y., et al. 2011, *MNRAS*, 412, 843
- Thompson, T. A. 2011, *ApJ*, 741, 82
- Tolstoy, E., Hill, V., & Tosi, M. 2009, *ARA&A*, 47, 371
- Torra, F., Castañeda, J., Fabricius, C., et al. 2021, *A&A*, 649, A10
- Tull, R. G., MacQueen, P. J., Sneden, C., & Lambert, D. L. 1995, *PASP*, 107, 251
- Vargas, L. C., Geha, M., Kirby, E. N., & Simon, J. D. 2013, *ApJ*, 767, 134
- Virtanen, P., Gommers, R., Oliphant, T. E., et al. 2020, *NatMe*, 17, 261
- Vogt, S. S., Allen, S. L., Bigelow, B. C., et al. 1994, *Proc. SPIE*, 2198, 362
- Webbink, R. F. 1984, *ApJ*, 277, 355
- Weisz, D. R., Dolphin, A. E., Skillman, E. D., et al. 2014, *ApJ*, 789, 147
- Wenger, M., Ochsenbein, F., Egret, D., et al. 2000, *A&AS*, 143, 9
- Whelan, J., & Iben, I. J. 1973, *ApJ*, 186, 1007
- Woosley, S. E., & Kasen, D. 2011, *ApJ*, 734, 38
- Woosley, S. E., Taam, R. E., & Weaver, T. A. 1986, *ApJ*, 301, 601
- Woosley, S. E., & Weaver, T. A. 1994, *ApJ*, 423, 371
- Woosley, S. E., & Weaver, T. A. 1995, *ApJS*, 101, 181
- Wright, E. L., Eisenhardt, P. R. M., Mainzer, A. K., et al. 2010, *AJ*, 140, 1868
- Yamada, S., Suda, T., Komiyama, Y., Aoki, W., & Fujimoto, M. Y. 2013, *MNRAS*, 436, 1362
- Yoon, S. C., Podsiadlowski, P., & Rosswog, S. 2007, *MNRAS*, 380, 933
- Zhang, H. W., & Zhao, G. 2005, *MNRAS*, 364, 712
- Zhao, G., Mashonkina, L., Yan, H. L., et al. 2016, *ApJ*, 833, 225
- Zwicky, F. 1958, *HDP*, 51, 766